PHYSICAL REVIEW D **88,** 044026 (2013)

Remnant massive neutron stars of binary neutron star mergers: Evolution process and gravitational waveform

Kenta Hotokezaka,[1] Kenta Kiuchi,[2] Koutarou Kyutoku,[3] Takayuki Muranushi,[2,4] Yu-ichiro Sekiguchi,[2] Masaru Shibata,[2] and Keisuke Taniguchi[5]

[1]*Department of Physics, Kyoto University, Kyoto 606-8502, Japan*
[2]*Yukawa Institute for Theoretical Physics, Kyoto University, Kyoto 606-8502, Japan*
[3]*Department of Physics, Universitiy of Wisconsin–Milwaukee, P.O. Box 413, Milwaukee, Wisconsin 53201, USA*
[4]*Hakubi Center for Advanced Research, Kyoto University, Kyoto 606-8501 Japan*
[5]*Graduate School of Arts and Sciences, The University of Tokyo, Tokyo 153-8902, Japan*

(Received 22 February 2013; published 16 August 2013)

Massive (hypermassive and supramassive) neutron stars are likely to be often formed after the merger of binary neutron stars. We explore the evolution process of the remnant massive neutron stars and gravitational waves emitted by them, based on numerical-relativity simulations for binary neutron star mergers employing a variety of equations of state and choosing a plausible range of the neutron star mass of binaries. We show that the lifetime of remnant hypermassive neutron stars depends strongly on the total binary mass and also on the equations of state. Gravitational waves emitted by the remnant massive neutron stars universally have a quasiperiodic nature of an approximately constant frequency although the frequency varies with time. We also show that the frequency and time-variation feature of gravitational waves depend strongly on the equations of state. We derive a fitting formula for the quasiperiodic gravitational waveforms, which may be used for the data analysis of a gravitational-wave signal.

DOI: 10.1103/PhysRevD.88.044026 PACS numbers: 04.25.D−, 04.30.−w, 04.40.Dg

I. INTRODUCTION

Coalescence of binary neutron stars is one of the most promising sources for next-generation, kilometer-size gravitational-wave detectors such as advanced LIGO, advanced VIRGO, and KAGRA [Large-scale Cryogenic Gravitational Wave Telescope (LCGT)] [1]. The first detection of gravitational waves will be achieved in the next ∼5 years by observing a chirp signal of gravitational waves emitted in the so-called inspiral stage in which binary neutron stars are in quasicircular orbits with orbital radius 30–700 km (the gravitational-wave frequency in the range ≈10–10^3 Hz). Statistical studies have predicted that the detection rate of gravitational waves for this signal will be ∼1–100 per year (e.g., [2,3]). After the first detection of gravitational waves from coalescence of a binary neutron star, it will be a great challenge to extract the information of matter effects from a gravitational-wave signal. For instance, a tidal deformability parameter will be measurable with the gravitational-wave signal during the inspiral stage [4].

After the merger of a binary neutron star sets in, there are two possible fates: If the total mass is large enough, a black hole is promptly formed, while if not, a massive neutron star (MNS) is formed. (Here, a massive neutron star means hypermassive or supramassive neutron star. See [5–7] for their definitions, respectively; see also Sec. II C.) Numerical-relativity simulations have shown that the threshold mass depends strongly on the equation of state (EOS) of the neutron star matter [8–12], which is sill poorly known to date [13]. However, the latest discoveries of high-mass neutron stars with mass $1.97 \pm 0.04 M_\odot$ [14] and $2.01 \pm 0.04 M_\odot$ [15] constrain that the maximum mass of (cold) spherical neutron stars for a given hypothetical EOS has to be larger than $\sim 2 M_\odot$. This suggests that the EOS of neutron stars has to be stiff; the pressure above the nuclear-matter density $\sim 2.8 \times 10^{14}$ g/cm^3 has to be sufficiently high. Motivated by this fact, we performed numerical-relativity simulations for a variety of stiff EOSs in previous papers [9,12], and found that a MNS is the universal outcome for the binary of a total mass smaller than the typical mass ~ 2.6–$2.8 M_\odot$. The purpose of this paper is to summarize our latest more systematic studies for the evolution process of the MNSs and quasiperiodic gravitational waves emitted by the MNSs formed after the merger of binary neutron stars.

In the past decade, the numerical simulation for the merger of binary neutron stars in full general relativity, which is the unique approach of the rigorous theoretical study for this subject, has been extensively performed since the first success in 2000 [16] (see, e.g., [17,18] for a review of this field). However, most of the simulations have been performed with simple polytropic EOSs (but see, e.g., [19–21] for the latest progress). For the detailed and physical study of the merger remnants and gravitational waves emitted by remnant MNSs, we have to employ physical EOSs. In the past two years, we have performed a number of simulations using piecewise polytropic EOSs [9,12] and tabulated finite-temperature EOSs taking into account a neutrino cooling process [10,11,22] for a variety of masses of binary systems (see also [23]). We now have a number of numerical results, a variety of the sample for remnant

MNSs, and possible gravitational waves emitted by them. By analyzing these samples, we can now summarize possible evolution processes of the remnant MNSs and the resulting gravitational waveforms. Furthermore, a variety of numerical gravitational waveforms enable us to construct an analytic model for such gravitational waveforms. In this paper, we report the results of our exploration for these issues.

The paper is organized as follows: In Sec. II, we summarize the EOSs employed in our latest numerical-relativity simulations, and models of binary neutron stars for which MNSs are formed. In Sec. III, we describe the properties and possible evolution processes of the MNSs. Section IV summarizes the properties of gravitational waves emitted by MNSs. Section V is devoted to deriving analytic formulas for modeling gravitational waves emitted by the MNSs. Section VI is devoted to a summary and discussion. Throughout this paper, we employ the geometrical units $c = 1 = G$ where c and G are the speed of light and gravitational constant, respectively, although we recover c when we need to clarify the units [24].

II. EQUATIONS OF STATE AND CHOSEN MODELS

A. Equations of state

In this section, we summarize the EOSs employed in our latest studies [10–12,22] and in the present work.

The exact EOS for the high-density nuclear matter is still unknown [13], and hence, a numerical simulation employing a single particular EOS, which might not be correct, would not yield a scientific result in this field. Simulations systematically employing a wide variety of possible hypothetical EOSs are required for exploring the merger of binary neutron stars. Nevertheless, the latest discoveries of a high-mass neutron star PSR J1614-2230 with mass $1.97 \pm 0.04 M_\odot$ [14] and PSR J0348 + 0432 with $2.01 \pm 0.04 M_\odot$ [15] significantly constrain the hypothetical EOSs to be chosen, because these suggest that the maximum allowed mass of (cold) spherical neutron stars for a given EOS (hereafter denoted by $M_{\rm max}$) has to be larger than $\sim 2 M_\odot$. This indicates that the EOS should be rather stiff, although there are still many candidate EOSs [13].

To this time, we have employed two types of EOSs. One is a piecewise polytropic EOS proposed by Read and her collaborators [25] (described below) and the other is a tabulated EOS in which finite-temperature effects together with the effects associated with the electron fraction per baryon is taken into account. In this study, we analyze numerical results [10] which were derived from a relativistic mean-field theory [26] assuming that neutron stars are composed of normal nuclear matter such as protons and neutrons. This EOS is stiff and yields $M_{\rm max} = 2.2 M_\odot$ (see Table I). We also employed the hyperonic version of Shen EOS [27] in [11]. However, this EOS is rather soft with $M_{\rm max} = 1.75 M_\odot$, and hence, we do not adopt the numerical results for this EOS in this paper.

The piecewise polytropic EOS is described assuming that neutron stars are cold (in a zero-temperature state); the rest-mass density ρ determines all other thermodynamical quantities. In the prescription of [25], there are the following four parameters: P_2: the pressure at $\rho := \rho_2 = 10^{14.7}$ g/cm^3 and $(\Gamma_1, \Gamma_2, \Gamma_3)$, the adiabatic indices that characterize the EOS for the nuclear matter (see, e.g., [12] for details). Table I lists parameters of the five piecewise polytropic EOSs which we employed and which are representative EOSs derived in nuclear theories. The values of $(P_2, \Gamma_1, \Gamma_2, \Gamma_3)$ are taken from [25]. The properties of these EOSs are described in [12] (see [28–32] for APR4, SLy, ALF2, H4, and MS1, respectively.)

Figure 1 plots the pressure as a function of the rest-mass density for five piecewise polytropic EOSs as well as for Shen EOS. APR4 and SLy have relatively small pressure for $\rho \lesssim \rho_3 := 10^{15}$ g/cm^3, while they have high pressure for $\rho \gtrsim \rho_3$. By contrast, H4, MS1, and Shen have pressure higher than APR4 and SLy for $\rho \lesssim \rho_3$, while they become softer for a high-density region $\rho \gtrsim \rho_3$. MS1 has the highest pressure for $\rho \lesssim \rho_3$ (i.e., the highest value of P_2) among many other EOSs, and thus, it is the stiffest EOS as far as the canonical neutron stars are concerned.

TABLE I. Parameters and key quantities for five piecewise polytropic EOSs and finite-temperature (Shen) EOSs employed so far. P_2 is shown in units of dyn/cm^2. $M_{\rm max}$ is the maximum mass along the sequences of cold spherical neutron stars. $(R_{1.35}, \rho_{1.35})$, $(R_{1.5}, \rho_{1.5})$, $(R_{1.6}, \rho_{1.6})$, and $(R_{1.8}, \rho_{1.8})$ are the circumferential radii in units of km and the central density in units of g/cm^3 for $1.35 M_\odot$, $1.5 M_\odot$, $1.6 M_\odot$, and $1.8 M_\odot$ neutron stars, respectively. We note that the values of the mass, radius, and density listed for the piecewise polytropic EOSs are slightly different from those obtained in the original tabulated EOSs (see the text for the reason). MS1 is referred to as this name in [25], but in other references (e.g., [13]), it is referred to as MS0. We follow [25] in this paper. The fitted parameters $(\log(P_2), \Gamma_1, \Gamma_2, \Gamma_3)$ are taken from [25].

EOS	$(\log(P_2), \Gamma_1, \Gamma_2, \Gamma_3)$	$M_{\rm max}\,(M_\odot)$	$R_{1.35}$	$\rho_{1.35}$	$R_{1.5}$	$\rho_{1.5}$	$R_{1.6}$	$\rho_{1.6}$	$R_{1.8}$	$\rho_{1.8}$
APR4	(34.269, 2.830, 3.445, 3.348)	2.20	11.1	8.9×10^{14}	11.1	9.6×10^{14}	11.1	10.1×10^{14}	11.0	11.4×10^{14}
SLy	(34.384, 3.005, 2.988, 2.851)	2.06	11.5	8.6×10^{14}	11.4	9.5×10^{14}	11.4	10.2×10^{14}	11.2	12.0×10^{14}
ALF2	(34.616, 4.070, 2.411, 1.890)	1.99	12.4	6.4×10^{14}	12.4	7.2×10^{14}	12.4	7.8×10^{14}	12.2	9.5×10^{14}
H4	(34.669, 2.909, 2.246, 2.144)	2.03	13.6	5.5×10^{14}	13.5	6.3×10^{14}	13.5	6.9×10^{14}	13.1	8.7×10^{14}
MS1	(34.858, 3.224, 3.033, 1.325)	2.77	14.4	4.2×10^{14}	14.5	4.5×10^{14}	14.6	4.7×10^{14}	14.6	5.1×10^{14}
Shen	(34.717, —, —, —)	2.20	14.5	4.4×10^{14}	14.4	4.9×10^{14}	14.4	5.8×10^{14}	14.2	6.7×10^{14}

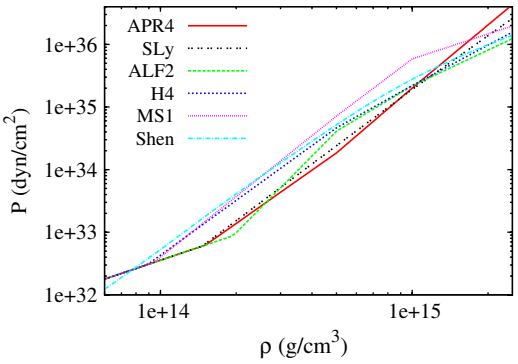

FIG. 1 (color online). Pressure as a function of the rest-mass density for the seven EOSs listed in Table I.

ALF2 has small pressure for $\rho \le \rho_2$ as in the case of APR4, but for $\rho_2 \lesssim \rho \le \rho_3$ the pressure is higher than that for APR4. For $\rho \ge \rho_2$ the pressure of ALF2 is as high as that for H4. The profile of Shen is similar to H4 although Shen has slightly higher pressure than H4 for a given value of the density. Also, APR4 and SLy are similar EOSs, but the slight difference between two EOSs results in a significant difference in the merger remnants for canonical-mass binary neutron stars (see Sec. III).

All the properties mentioned above are reflected in the radius $R_{1.35}$ and central density $\rho_{1.35}$ of (cold) spherical neutron stars with the canonical mass $M = 1.35M_\odot$ [33] where M is the gravitational [Arnowitt-Deser-Misner (ADM)] mass of the cold spherical neutron stars in isolation; see Table I. The pressure at $\rho = \rho_2$ (i.e., P_2) is correlated well with this radius and central density [34] (see also below).

In the numerical simulation, we used a modified version of the piecewise polytropic EOS to approximately take into account thermal effects. In this EOS, the pressure and specific internal energy are decomposed into cold and thermal parts as

$$P = P_{\rm cold} + P_{\rm th}, \qquad \varepsilon = \varepsilon_{\rm cold} + \varepsilon_{\rm th}. \tag{1}$$

The cold parts of both variables are calculated using the original piecewise polytropic EOS from the primitive variable ρ, and then the thermal part of the specific internal energy is defined from ε as $\varepsilon_{\rm th} = \varepsilon - \varepsilon_{\rm cold}(\rho)$. Because $\varepsilon_{\rm th}$ vanishes in the absence of shock heating, it is regarded as the finite-temperature part determined by the shock heating in the present context. For the thermal part of the pressure and specific internal energy, a Γ-law ideal-gas EOS was adopted as

$$P_{\rm th} = (\Gamma_{\rm th} - 1)\rho\varepsilon_{\rm th}. \tag{2}$$

Following the conclusion of a detailed study in [35], $\Gamma_{\rm th}$ is chosen in the range 1.6–2.0 with the canonical value 1.8. For several models, simulations were performed varying the value of $\Gamma_{\rm th}$ (see Table II).

B. Models

Numerical simulations were performed for a variety of EOSs and for many sets of masses of binary neutron stars. Because the mass of each neutron star in the observed binary systems is in a narrow range between $\sim$1.23–1.45$M_\odot$ [33], we basically choose the neutron star masses 1.20, 1.25, 1.30, 1.35, 1.40, 1.45, and 1.5$M_\odot$ with the canonical mass 1.35$M_\odot$ (the canonical total mass $m = m_1 + m_2 = 2.7M_\odot$). Also, the mass ratio of the observed system $q := m_1/m_2 (\le 1)$ where m_1 and m_2 denote the mass of lighter and heavier neutron stars, respectively, is in a narrow range $\sim$0.85–1. Thus, we choose q as $0.8 \le q \le 1$. The models employed in the present analysis are listed in Table II. In the following, we specify the model by the names listed in this table. We note that for APR4 and SLy, a black hole is formed promptly after the onset of the merger for $m \ge 2.9M_\odot$ and $m \ge 2.8M_\odot$, respectively. (Although they are not listed in Table II, we performed a simulation for $m_1 = m_2 = 1.4M_\odot$ with SLy and three simulations for $m = 2.9M_\odot$ with APR4.)

We found that for models with $m \le 2.7M_\odot$, MNSs were always formed irrespective of the EOSs employed. Even for $m = 2.8M_\odot$, MNSs were formed for all the EOSs except for SLy. For stiffer EOSs, MNSs can be formed even for $m = 3M_\odot$ (e.g., for Shen and MS1 EOSs). Thus, for H4, MS1, and Shen, we performed simulations for higher-mass models with $m_2 = 1.6M_\odot$. The models in which MNSs are formed are summarized in Table II. In Secs. III and IV, we will analyze the evolution process of the MNSs and the waveform of emitted gravitational waves, derived for these models.

Numerical simulations with the piecewise polytropic EOSs were performed using an adaptive-mesh refinement code SACRA [36]. For these simulations, the semimajor diameter of neutron stars is initially covered by $\approx$100 grid points (we refer to this grid resolution as high resolution). We also performed lower-resolution simulations covering the the semimajor axis by $\approx$65 and 80 grid points (we refer to these grid resolutions as low and middle resolutions). The accuracy and convergence of the numerical results for the high grid resolution is found in [12] and in the Appendix; e.g., the averaged frequency of gravitational waves emitted from MNSs is determined within $\sim$0.1 kHz error. Numerical simulations with Shen EOS were performed using a code developed in [10,11]. For these simulations, the semimajor diameter of neutron stars is initially covered by $\approx$80 grid points. The accuracy and convergence of the numerical results for the high grid resolution would be slightly poorer than those in the piecewise polytropic EOS case. For comparison, we performed simulations using these two codes with the same total mass and EOS, H4-135135. Then, we found that the averaged frequency of gravitational waves emitted by hypermassive neutron stars (HMNS) agrees with each other within 1% accuracy. For all these simulations, the initial data were

TABLE II. List of the simulation models in which a MNS is formed. The model is referred to as the name "EOS"-"m_1," "m_2;" e.g., the model employing APR4, $m_1 = 1.3M_\odot$, and $m_2 = 1.4M_\odot$ is referred to as model APR4-130140. The second–fourth columns show the adiabatic index for the thermal pressure for the piecewise polytropic EOS and masses of two components. The last three columns show the numerical results, approximate lifetime of the MNS that was found in our simulation time, the rest mass of disks surrounding the remnant black hole, and final gravitational mass of the system. The — denotes that the lifetime of the MNS is much longer than 30 ms and we did not find a black-hole formation in our simulation time. The disk mass is measured at 10 ms after the formation of the black hole. We note that a black hole is formed soon after the onset of the merger with $m \geq 2.9M_\odot$ for APR4 and with $m \geq 2.8M_\odot$ for SLy. For ALF2 with $m = 2.9M_\odot$, a MNS is formed after the merger but its lifetime is quite short, <5 ms.

Model	$\Gamma_{\rm th}$	m_1 ($M_\odot$)	m_2 ($M_\odot$)	Lifetime (ms)	Disk mass ($M_\odot$)	Final mass ($M_\odot$)
APR4-130150	1.8	1.30	1.50	30	0.12	2.69
APR4-140140	1.8	1.30	1.50	35	0.12	2.69
APR4-120150	1.6, 1.8, 2.0	1.20	1.50	—	—	2.60, 2.59, 2.59
APR4-125145	1.8	1.25	1.45	—	—	2.60
APR4-130140	1.8	1.30	1.40	—	—	2.60
APR4-135135	1.6, 1.8, 2.0	1.35	1.35	—	—	2.59, 2.61, 2.60
APR4-120140	1.8	1.20	1.40	—	—	2.52
APR4-125135	1.8	1.25	1.35	—	—	2.53
APR4-130130	1.8	1.30	1.30	—	—	2.53
SLy-120150	1.8	1.20	1.50	10	0.12	2.60
SLy-125145	1.8	1.25	1.45	15	0.14	2.60
SLy-130140	1.8	1.30	1.40	15	0.11	2.60
SLy-135135	1.8	1.35	1.35	10	0.08	2.58
SLy-130130	1.8	1.30	1.30	—	—	2.51
ALF2-145145	1.8	1.45	1.45	2	0.04	2.84
ALF2-140140	1.8	1.40	1.40	5	0.07	2.72
ALF2-120150	1.8	1.20	1.50	45	0.31	2.63
ALF2-125145	1.8	1.25	1.25	40	0.23	2.63
ALF2-130140	1.8	1.30	1.40	10	0.12	2.63
ALF2-135135	1.8	1.35	1.35	15	0.17	2.62
ALF2-130130	1.8	1.30	1.30	—	—	2.54
H4-130160	1.8	1.30	1.60	5	0.12	2.83
H4-145145	1.8	1.45	1.45	5	0.03	2.81
H4-130150	1.8	1.30	1.50	20	0.25	2.72
H4-140140	1.8	1.40	1.40	10	0.03	2.72
H4-120150	1.6, 1.8, 2.0	1.20	1.50	—	—	2.65, 2.64, 2.64
H4-125145	1.8	1.25	1.25	—	—	2.63
H4-130140	1.8	1.30	1.40	—	—	2.62
H4-135135	1.6, 1.8, 2.0	1.35	1.35	15, 25, 35	0.08, 0.08, 0.08	2.62, 2.62, 2.62
H4-120140	1.8	1.30	1.30	—	—	2.54
H4-125135	1.8	1.30	1.30	—	—	2.55
H4-130130	1.8	1.30	1.30	—	—	2.53
MS1-130160	1.8	1.30	1.60	—	—	2.85
MS1-145145	1.8	1.45	1.45	—	—	2.85
MS1-140140	1.8	1.40	1.40	—	—	2.75
MS1-120150	1.8	1.20	1.50	—	—	2.65
MS1-125145	1.8	1.25	1.25	—	—	2.66
MS1-130140	1.8	1.30	1.40	—	—	2.66
MS1-135135	1.8	1.35	1.35	—	—	2.65
MS1-130130	1.8	1.30	1.30	—	—	2.56
Shen-120150	—	1.20	1.50	—	—	2.64
Shen-125145	—	1.25	1.45	—	—	2.61
Shen-130140	—	1.30	1.40	—	—	2.63
Shen-135135	—	1.35	1.35	—	—	2.62
Shen-140140	—	1.40	1.40	—	—	2.74
Shen-150150	—	1.50	1.50	—	—	2.95
Shen-160160	—	1.60	1.60	10	0.10	3.12

prepared by a code described in [37], which was developed from the LORENE library [38].

C. Hypermassive and supramassive neutron stars

Before going ahead, we remind the readers the definitions of the hypermassive [5] and supramassive neutron stars [6,7]. We note that in the definitions, we suppose that neutron stars are cold (i.e., finite-temperature effects are negligible).

A sequence of spherical neutron stars always has the maximum mass state. Rotation can increase the maximum mass of neutron stars. The maximum mass of a *uniformly* rotating neutron star (hereafter denoted by $M_{\rm max,s}$) is determined by the spin rate at which the mass element at the equator rotates with the (general relativistic) Kepler velocity and further speedup would lead to mass shedding. This maximum mass for cold neutron stars was determined numerically for a variety of nuclear-theory-based EOSs in [7], which shows that $M_{\rm max,s}$ is by 15%–20% larger than $M_{\rm max}$. For stiff EOSs in which $M_{\rm max} > 2M_\odot$, it is empirically known that this increase factor is $\sim$20%. Rotating neutron stars with their rest mass exceeding the maximum rest mass of nonspinning neutron stars for a given EOS are referred to as supramassive neutron stars (SMNSs) [6]. A uniformly rotating (cold) neutron star with mass exceeding $\approx M_{\rm max,s}$ will collapse to a black hole. However, a uniformly rotating (cold) neutron star with mass between $M_{\rm max}$ and $M_{\rm max,s}$ may be alive, and it will collapse to a black hole only for the case that a process for the dissipation of its angular momentum is present. The typical dissipation process is an electromagnetic emission such as magnetic dipole radiation, for which the dissipation time scale is much longer than 1 s for the typical magnetic-field strength $\sim 10^{12}$ G and the allowed spin period ($\gtrsim 1$ ms) of the neutron stars.

The merger of binary neutron stars does not result, in general, in a uniformly rotating remnant, but in a *differentially* rotating one. The inner region of the remnant MNSs often rotates faster than the envelope: The angular velocity in the inner region can be larger than the Kepler one of the equator as first found in [16]. This implies that the centrifugal force, which can have the significant contribution to supporting the strong self-gravity of the merger remnant, is enhanced, and thus, the maximum allowed mass of the remnant MNS can exceed the maximum allowed mass of SMNSs for a given EOS, $M_{\rm max,s}$. Such differentially rotating neutron stars with their mass exceeding $M_{\rm max,s}$ are referred to as HMNSs. Therefore, a differentially rotating (cold) neutron star with mass exceeding $\approx M_{\rm max,s}$ does not always have to collapse to a black hole.

The left side of Fig. 2 schematically shows the definition of the HMNS and SMNS. The neutron stars with the mass smaller than $M_{\rm max}$ are referred to as normal neutron stars in this figure.

If the degrees of the differential rotation is significantly reduced by some angular-momentum transport or

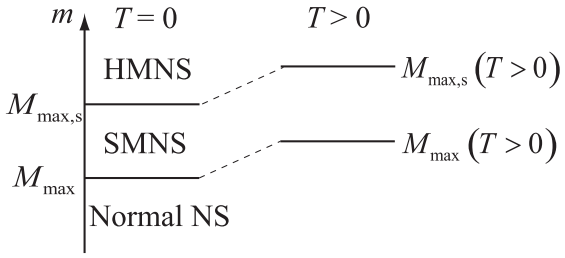

FIG. 2. A schematic diagram for explaining HMNS and SMNS. $M_{\rm max}$ has to be larger than $\sim 2M_\odot$ and for such stiff EOSs, we empirically know that $M_{\rm max,s} \approx 1.2M_{\rm max}$ [7]. T denotes the typical temperature of MNS. See the text for details.

dissipation processes, HMNSs will be unstable against gravitational collapse. There are several possible processes for transporting angular momentum (e.g., [39–41]). One is the purely hydrodynamics effect. This becomes an efficient process for HMNSs formed soon after the merger of binary neutron stars, because such HMNSs usually have a nonaxisymmetric structure and exert the torque to the matter in the envelope. Then, the angular momentum in the inner part of the HMNSs is transported outward, and as the decrease of the angular momentum in the inner part, the degrees of the differential rotation is reduced. In the present simulations as well as our simulations of [10–12], only this process is taken into account, but this is really an efficient process in particular for the early evolution stage of the HMNSs in which the degrees of nonaxisymmetry is quite high.

There are two other possible effects for the angular-momentum transport, both of which are activated in the presence of magnetic fields. One is the magnetic winding effect (e.g., [5]) for which the order of the angular-momentum transport time scale is

$$\tau_{\rm wind} \sim \frac{R}{v_A} \sim 10^2 \rho_{15}^{1/2} B_{15}^{-1} R_6 \ {\rm ms}, \tag{3}$$

where R is the typical radius of the HMNS with $R_6 = R/(10^6\ {\rm cm})$, and v_A is the Alfvén velocity

$$v_A \approx \frac{B}{\sqrt{4\pi\rho}}. \tag{4}$$

Here, B is the typical magnitude of the radial component of magnetic fields with $B_{15} = B/(10^{15}\ {\rm G})$, and ρ is the typical density with $\rho_{15} = \rho/(10^{15}\ {\rm g/cm^3})$. Thus, for the sufficiently high magnetic-field strength which could be yielded by the winding itself and compression, the angular-momentum transport is significantly enhanced.

The other mechanism is the magnetorotational instability (MRI) [42,43] by which an effective viscosity is likely to be generated with the effective viscous parameter

$$\nu_{\rm vis} \sim \alpha_{\rm vis} \frac{c_s^2}{\Omega}, \tag{5}$$

where $\alpha_{\rm vis}$ is the so-called α parameter which will be 0.01–0.1 [43], c_s is the typical sound velocity of order $\sim 0.1c$, and Ω is the typical angular velocity $\sim 10^4$ rad/s with $\Omega_4 = \Omega/(10^4\ {\rm rad/s})$. Thus, the viscous

angular-momentum transport time scale in the presence of magnetic fields would be

$$\tau_{\rm mri} \sim \frac{R^2}{\nu_{\rm vis}} \sim 10^2 R_6^2 \Omega_4 \left(\frac{\alpha_{\rm vis}}{10^{-2}}\right)^{-1} \left(\frac{c_s}{0.1c}\right)^{-2} \ {\rm ms}, \quad (6)$$

and hence, the time scale is as short as $\tau_{\rm wind}$ for the hypothetical radial field strength $B_{15} \gtrsim 1$. Both effects work as long as differential rotation is present even in the absence of nonaxisymmetry. Therefore, unless any process stabilizes them, HMNSs with sufficiently high mass would collapse to a black hole in the time scale, $\tau_{\rm wind}$ or $\tau_{\rm mri}$, which is $\sim 10^2$ ms.

In the definitions of HMNS and SMNS described above, we have not considered finite-temperature (thermal) effects. This effect could be important for the remnant MNS of binary neutron stars [44]. The reason for this is that during the merger process, strong shocks are often formed and the maximum temperature of MNSs is increased up to 30–50 MeV [10,11]. The thermal pressure associated with this high temperature is several 10% of the cold-part pressure caused by the repulsive nuclear force, and hence, it is never negligible. Although it is not easy to strictly determine their values, it is reasonable to consider that the finite-temperature effect could increase the values of $M_{\rm max}$ and $M_{\rm max,s}$ by $\sim 0.1 M_\odot$. The right-hand side of Fig. 2 schematically shows the possible increase of these values. Hereafter we refer to these values as $M_{\rm max}(T>0)$ and $M_{\rm max,s}(T>0)$, supposing that these are larger than $M_{\rm max}$ and $M_{\rm max,s}$ by $\sim 0.1 M_\odot$.

The finite-temperature neutron stars will eventually dissipate the thermal energy in a short time scale $\sim$1–10 s because of the neutrino cooling [43]. References [10,11] indeed show that the time scale of the neutrino emission is of order seconds. Here, when we consider the possible evolution processes of HMNS and SMNS, we have to keep in mind that in this time scale, the values of $M_{\rm max}(T>0)$ and $M_{\rm max,s}(T>0)$ could be by $\sim 0.1 M_\odot$ larger than $M_{\rm max}$ and $M_{\rm max,s}$. For example, consider a differentially rotating and hot remnant MNS for which the mass is larger than $M_{\rm max,s}$ and smaller than $M_{\rm max,s}(T>0)$. If a process of angular-momentum transport works and the degrees of differential rotation is significantly reduced, such a remnant will be unstable against gravitational collapse for the case that the thermal effect is negligible. However, if the thermal effect is important even after the angular-momentum transport process works, it will be stable in the cooling time scale. It will eventually collapse to a black hole after the neutrino cooling. However, its lifetime $\gtrsim 1$ s could be much longer than the angular-momentum transport time scale $\lesssim 100$ ms.

III. PROPERTIES AND EVOLUTION PROCESS OF MNS

Previous studies (e.g., [9,10,12]) clarified that soon after the onset of the merger, either a long-lived MNS (HMNS or SMNS or normal neutron star) or a black hole is formed. For most of the simulations in this paper performed with stiff EOSs and with the canonical total mass 2.6–2.8$M_\odot$, we found that a long-lived MNS is formed with its lifetime much longer than its dynamical time scale $\sim$0.1 ms and its rotation period $\sim$1 ms (cf. Figs. 3–5). The unique properties to be particularly noticed are that the MNSs are rapidly and differentially rotating, and nonaxisymmetric (cf. Figs. 4 and 5): Thus, they could be temporarily stable even if they are very massive, and in addition, they could be strong sources of gravitational waves. The purpose of this section is to explore the properties and evolution processes of such MNSs. In the subsequent sections, we will clarify the properties of gravitational waves.

A. Dependence on EOS

Figure 3 plots the evolution of the maximum density for five piecewise polytropic EOSs and the Shen EOS with several binary masses in the range $m = 2.6M_\odot$–$2.8M_\odot$. For Shen and MS1 EOSs, the results with more massive cases are also plotted. This figure shows that the evolution process of MNSs depends strongly on the EOSs and total mass as described in the following.

APR4: For this EOS, the pressure at $\rho = \rho_2$ (i.e., the value of P_2) is lowest among all the EOSs employed. However, the pressure for $\rho \geq \rho_3$ is rather high because the adiabatic index for this density range (i.e., Γ_3) is highest. Reflecting the small pressure for $\rho < \rho_3$, the maximum density increases steeply during the early stage of the merger due to the sudden increasing strength of the self-gravity. However, also, reflecting the high pressure for $\rho > \rho_3$ due to the high value of Γ_3, the steep increase of the density is hung up and subsequently the maximum density oscillates with high amplitude for several oscillation periods (for $\sim$5 ms). This is the unique feature for this type of EOS (i.e., APR4 and SLy). After a subsequent relaxation process through the interaction with the envelope surrounding the central core, the maximum density eventually relaxes approximately to a constant.

In this relaxation process, the angular momentum is transported substantially from the inner region to the outer region via the hydrodynamical angular-momentum transport process, because the MNS has a highly nonaxisymmetric structure and can exert the torque to the surrounding matter in its early evolution stage. It is worthy to note that the high-amplitude oscillation also plays an important role for enhancing the angular-momentum transport because the MNS interacts directly with the envelope during this oscillation.

The resulting MNSs formed after the relaxation evolve in a quasistationary manner. For a relatively small total mass with $m \lesssim 2.7M_\odot$, the maximum density in the quasistationary stage remains approximately constant for a sufficiently long time $\gg 10$ ms. This is due to the fact that the gravitational-wave emission does not yield significant

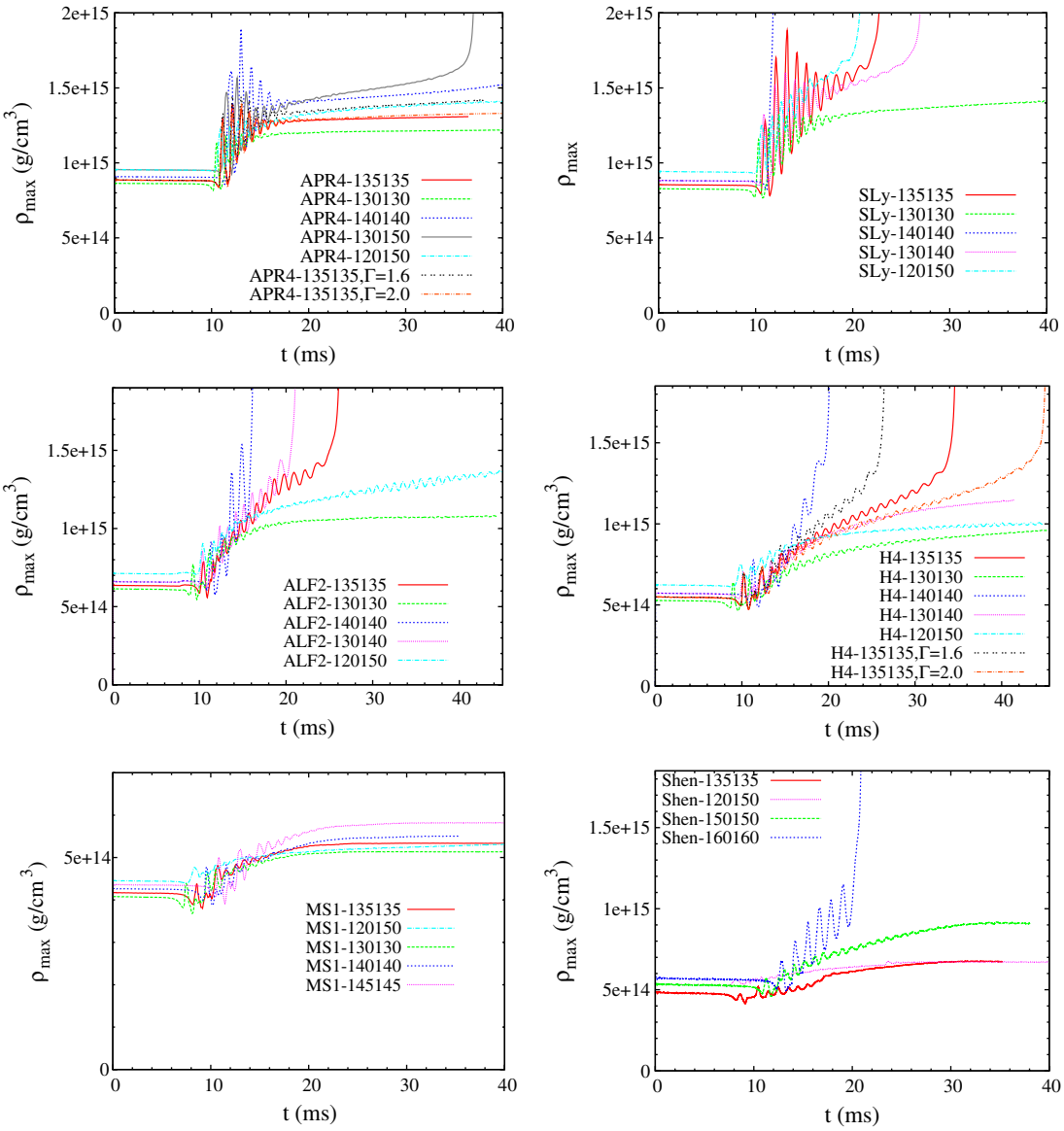

FIG. 3 (color online). Maximum density as a function of time for APR4 (top left), SLy (top right), ALF2 (middle left), H4 (middle right), MS1 (bottom left), and Shen (bottom right) EOSs with several values of binary mass. Note that Γ for the panel of APR4 and ALF2 denotes $\Gamma_{\rm th}$ and the absence of the Γ value means that $\Gamma_{\rm th} = 1.8$. For APR4-140140 and ALF2-120150, we confirmed that a black hole was eventually formed at $t \sim 47$ and 52 ms.

dissipation, i.e., the system relaxes to a quasistationary state for this stage, and that the final mass of the MNS is likely to be smaller than $M_{\rm max,s}$ or $M_{\rm max,s}(T > 0)$. The first fact can be found by estimating the dissipation time scale by the gravitational-wave emission which is much longer than the dynamical time scale (see also Figs. 7–9 from which we find that gravitational-wave amplitude for the $t - t_{\rm merge} > 10$ ms is much smaller than that for $t - t_{\rm merge} \lesssim 5$ ms). To confirm the second fact, we calculated the final gravitational mass of the system applying the formula of the ADM mass for a finite sphere of radius $\approx$300 km (see Table II) which is approximately equal to the initial ADM mass minus the energy carried out by gravitational waves, and found that for $m = 2.6M_\odot$ and $2.7M_\odot$, the final mass is $\approx 2.53M_\odot$ and $2.60M_\odot$, respectively. The value of $M_{\rm max}$ for this EOS is $\approx 2.20M_\odot$, and thus, that of $M_{\rm max,s}$ should be $\sim 2.6M_\odot$ according to the numerical results of [7]. Then, it is reasonable to consider that the value of $M_{\rm max,s}(T > 0)$ is larger than $2.6M_\odot$. Therefore, for $m = 2.6M_\odot$, the remnant is a SMNS, and hence, it will be alive for a long time $\gg 1$ s, even in the presence of a realistic process of the angular-momentum transport and dissipation (see Sec. II C), and for $m = 2.7M_\odot$, the remnants may be HMNSs. However, the mass would be smaller than $M_{\rm max,s}(T > 0)$. For this system, the angular-momentum transport alone may not trigger the

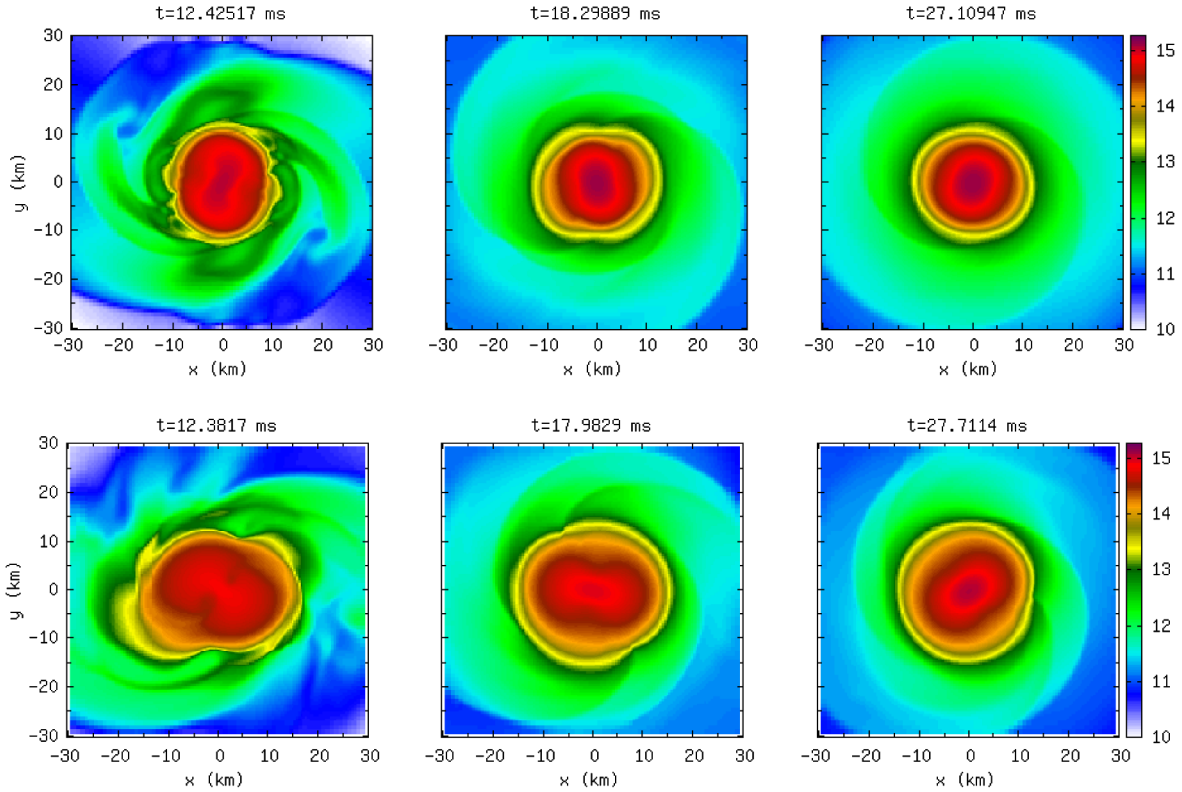

FIG. 4 (color online). Snapshots of the density profile in the equatorial plane at selected time slices for equal-mass models APR4-135135 (upper panels) and H4-135135 (lower panels) with $\Gamma_{\rm th} = 1.8$.

gravitational collapse, and the lifetime of the HMNS would be determined by the neutrino cooling in reality.

For $m \gtrsim 2.8M_\odot$, on the other hand, the remnants are HMNSs which evolve due to the gravitational-wave emission and hydrodynamical angular-momentum transport, resulting in the slow but monotonic increase of the maximum density with time for the quasistationary stage. For example, for APR4-130150 and APR4-140140, a black hole is formed at $\sim$30 and 35 ms after the onset of the merger in our simulations. The resulting object is a black hole surrounded by a massive disk (or torus) of mass $\sim 0.1M_\odot$. Here, the high mass of the disk is a result of the long-term angular-momentum transport process in the HMNS stage.

SLy: For this EOS, the evolution process agrees qualitatively with that for APR4. However, the value of $M_{\rm max}$ for this EOS is slightly (by $0.14M_\odot$) smaller than that for APR4. Thus, the values of $M_{\rm max,s}$ and $M_{\rm max,s}(T > 0)$ would be also smaller by $\sim 0.15M_\odot$; the plausible value of $M_{\rm max,s}$ would be $\sim 2.45M_\odot$. Reflecting this fact, the threshold mass for the prompt formation of the black hole becomes $m \approx 2.8M_\odot$ for this EOS. For $m = 2.7M_\odot$ with which the mass of the remnant MNS is $\sim 2.6M_\odot > M_{\rm max,s}$ and thus the MNS is hypermassive, a black hole is formed in $\sim$10–15 ms after the onset of the merger irrespective of the mass ratio; the lifetime of the HMNS is not very long. For $m = 2.6M_\odot$, the mass of the remnant MNS is $\gtrsim 2.5M_\odot$, and thus, the MNS is hypermassive as well. However, for this mass, the lifetime is $\gg 10$ ms; the gravitational-wave emission and hydrodynamical angular-momentum transport process also are not sufficient for inducing the collapse. Subsequent evolution of such a HMNS will be determined by angular-momentum transport processes or cooling in reality. If the thermal pressure plays a sufficiently important role, the HMNS collapses to a black hole after the neutrino cooling with the time scale of seconds, and if it does not, the collapse to a black hole occurs in some angular-momentum transport time scale $\sim$100 ms.

As argued in the following, binary neutron stars with $m = 2.8M_\odot$ do not result in a black-hole formation promptly after the onset of the merger for ALF2 and H4 EOSs for which the value of $M_{\rm max} \sim 2M_\odot$, by contrast to the case of SLy. This suggests that for a given value of $M_{\rm max}$, the black-hole formation is more subject to EOSs with smaller values of P_2, or in other words, with smaller radii of canonical-mass neutron stars. As shown in Sec. IV, a characteristic peak in the Fourier spectrum of gravitational waves for a high-frequency band $\sim$2–4 kHz is present for the case that a MNS is formed after the merger. This implies that if high-frequency gravitational waves from the merger of binary neutron stars with particular total mass, say $2.8M_\odot$, are observed, we will be able to constrain the EOS of neutron stars only by determining whether the peak is present or not [45].

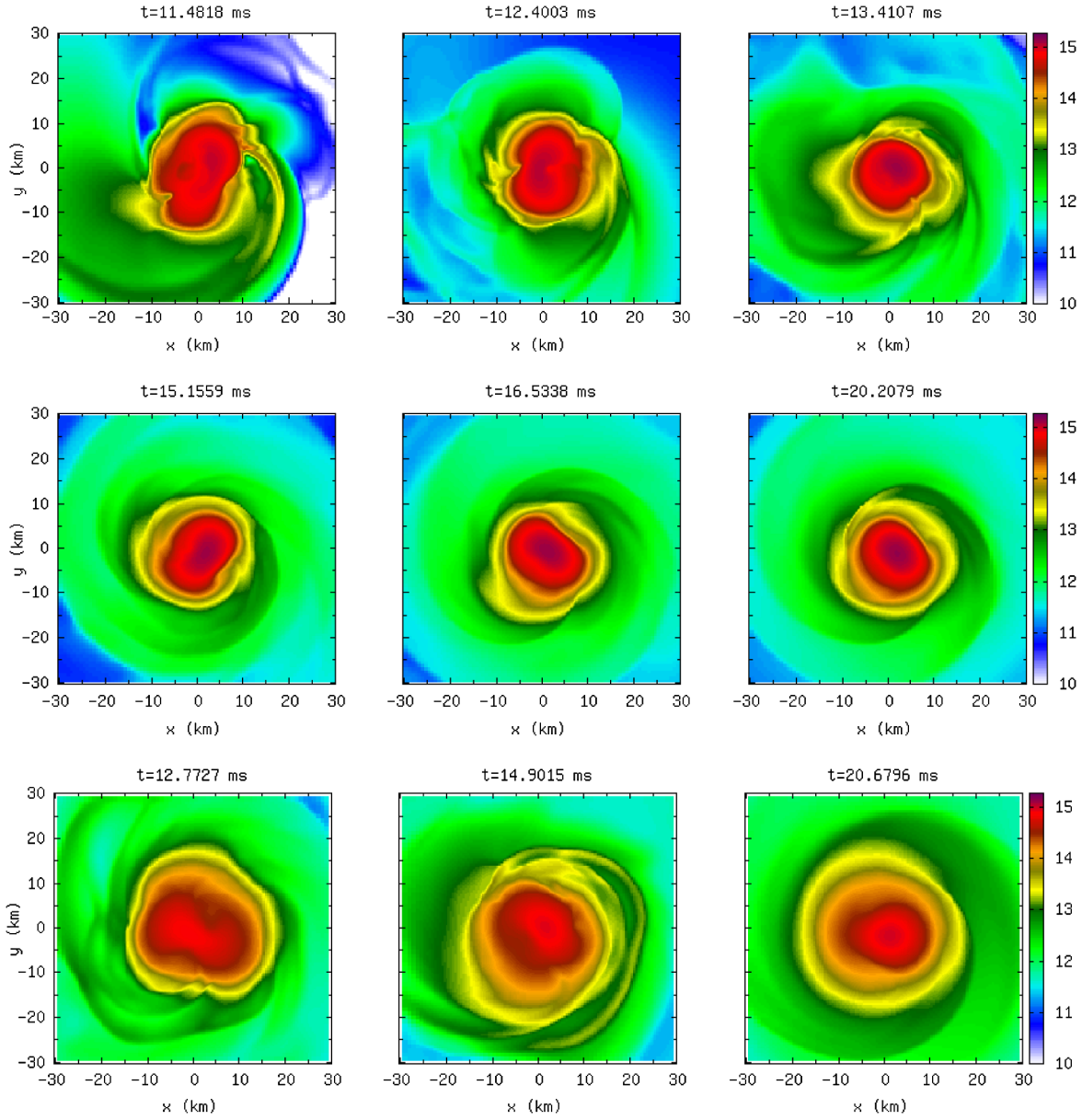

FIG. 5 (color online). The same as Fig. 4 but for unequal-mass models APR4-120150 (upper and middle panels) and H4-120150 (bottom panels).

ALF2: For this EOS, not only neutron stars of mass 1.2–1.5$M_\odot$ but also MNSs just after the formation with $m =$ 2.6–2.8$M_\odot$ have the maximum density between ρ_2 and ρ_3. Thus, although the oscillation of the maximum density is observed, its amplitude is not as high as that for APR4 and SLy, and hence, the angular-momentum transport process does not seem to be as efficient as for APR4 and SLy as well. For ALF2, however, the adiabatic index for this density range is small ($\Gamma_2 \sim 2.4$), although the pressure for $\rho_2 \leq \rho \leq \rho_3$ is relatively high. Because of this property, the maximum density of the MNSs increases as a result of the gravitational radiation reaction and hydrodynamical angular-momentum transport with a relatively short time scale. For the models with $m \gtrsim 2.7M_\odot$, the maximum density becomes eventually larger than ρ_3. For $\rho > \rho_3$, the adiabatic index is quite small ($\Gamma_3 \sim 1.9$), and hence, the increase of the maximum density is enhanced, leading to the eventual gravitational collapse to a black hole. For this evolution process, the formation time scale of the black hole is determined by the time scale of gravitational-wave emission or hydrodynamical angular-momentum transport.

For $m = 2.7M_\odot$ and $2.8M_\odot$, the remnant mass is $\approx 2.63M_\odot$ and $2.72M_\odot$, and thus, the remnants are very hypermassive, because for this EOS, $M_{\rm max} \approx 2.0M_\odot$ and $M_{\rm max,s}$ would be $\lesssim 2.4M_\odot$. Since the black hole is formed for $m \geq 2.7M_\odot$, the thermal pressure is not sufficient for sustaining the additional self-gravity of the HMNSs; $M_{\rm max,s}(T > 0) - M_{\rm max,s}$ would be smaller than $\sim 0.2M_\odot$.

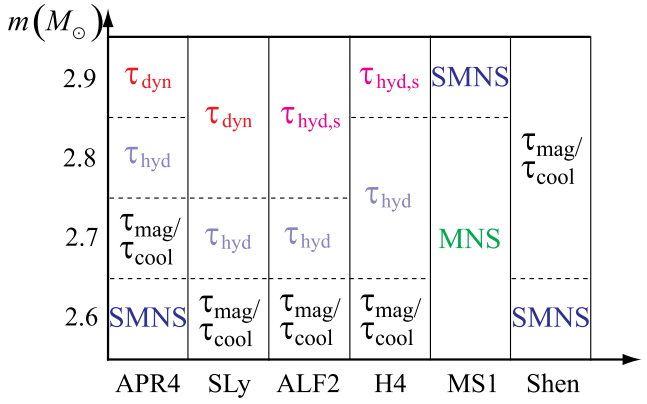

FIG. 6 (color online). The evolution time scale of the system in the plane composed of EOSs and total mass. τ_{dyn}: A black hole is formed in the dynamical time scale after the onset of the merger. τ_{hyd}: A HMNS is formed and its lifetime is determined by the hydrodynamical angular-momentum transport time scale. $\tau_{hyd,s}$: The same as for τ_{hyd} but the lifetime is shorter than $\sim$10 ms. τ_{mag}/τ_{cool}: A HMNS is formed and its lifetime would be determined by the time scale of angular-momentum transport by some magnetohydrodynamics effects or by the neutrino cooling time scale. The evolution time scale for a given total mass depends weakly on the mass ratio. For MS1, only the MNS or SMNS is formed for $m \leq 2.9M_\odot$. For APR4 and Shen, the remnant for the $m \lesssim 2.6M_\odot$ case is likely to be a SMNS (not HMNS).

For relatively small mass $m = 2.6M_\odot$, on the other hand, the emission of gravitational waves and hydrodynamical angular-momentum transport become inactive before the maximum density significantly exceeds ρ_3. In this case, the increase of the maximum density is stopped and the HMNS relaxes to a quasistationary state. The resulting remnant mass is $\approx 2.54M_\odot$ which is likely to be larger than $M_{max,s}$. Thus, the remnant is likely to be a HMNS. Subsequent evolution of such HMNS will be determined by angular-momentum transport processes or cooling in reality, as in the case of model SLy-130130.

One point worthy to be noted is that the evolution process for $m = 2.7M_\odot$ depends on the mass ratio (compare the plots for ALF2-135135 and ALF2-120150). For the sufficiently large asymmetry (i.e., $q = 0.8$), the lifetime of the HMNS becomes much longer than that of the equal-mass model for this EOS. The reason is that for the asymmetric case, the merger occurs at a larger orbital separation than for the equal-mass case; i.e., before a sufficient amount of angular momentum is dissipated by the gravitational-wave emission, the merger sets in. In addition, a large fraction of the materials (in particular the materials of the less-massive neutron star) obtain a sufficient angular momentum during the merger process resulting in a disk or a material ejected from the system [12]. This reduces the mass of the HMNS and the collapse to a black hole is delayed [46].

H4: The evolution process of MNSs in this EOS is similar to that in ALF2. As the value of M_{max} is approximately equal to that in ALF2, the criterion for the MNS formation is also very similar. For this EOS, however, the adiabatic index does not decrease with the increase of the density as drastically as for ALF2. Thus, the increase rate of the maximum density with time is relatively slow, and reflecting this fact, the configuration of the MNS relaxes to a quasistationary one in a short time scale after its formation. The resulting quasistationary MNS evolves through the hydrodynamical angular-momentum transport process and gravitational-wave emission subsequently. However the evolution time scale is much longer than 10 ms.

A point clearly seen for the density-evolution plot of this EOS is that the difference in the shock-heating efficiency (i.e., the value of Γ_{th}) is reflected in the change of the lifetime of the HMNSs: By the increasing efficiency of the shock heating (for the larger values of Γ_{th}), the lifetime of the HMNSs becomes longer (this effect should be universally found irrespective of the EOSs). It is also found that the presence of the mass asymmetry increases the lifetime of the HMNS because a large fraction of the materials escapes from the HMNS during the early stage of the merger for this EOS.

MS1: For this EOS, the maximum mass of spherical neutron stars is too high ($M_{max} \approx 2.77M_\odot$) to form SMNSs or HMNSs for $m \leq 2.8M_\odot$ because the remnant mass for such initial mass range is smaller than $2.75M_\odot$ (see Table II). For this case, the merger remnant relaxes to a quasistationary MNS in a time scale $\sim$10–15 ms. In a real MNS, a dissipation or a transport process of the angular momentum plays a role for the subsequent evolution for it. However, a black hole will not be formed for $m \leq 2.8M_\odot$ for which the remnant mass is smaller than $M_{max} \approx 2.77M_\odot$. For $m = 2.9M_\odot$, a quasistationary MNS is also formed. For this case, the MNS is likely to be supramassive, but not hypermassive. Thus, this MNS will be also alive for a long time scale $\gg 1$ s.

Shen: The evolution process of MNSs in this EOS is similar to that in H4, although the threshold mass for the eventual formation of a black hole is much higher than that for H4 ($m > 3.0M_\odot$ while $m \gtrsim 2.7M_\odot$ for H4). For this EOS, a long-lived HMNS is formed even for $m = 3.0M_\odot$ which is by 36% larger than the value of $M_{max} \approx 2.2M_\odot$. By contrast, for H4, a black hole is eventually formed if $m \gtrsim 2.7M_\odot \approx 1.33M_{max}$. This suggests that in the tabulated EOS in which the heating effects are taken into account in a more strict way, the shock heating may play a more important role for sustaining the self-gravity of the HMNS.

Before closing this section, it is worthy to summarize the dependence of the evolution process for MNSs of canonical mass $m \approx 2.7M_\odot$ on EOSs as follows:

(i) For the EOSs such as APR4 and SLy for which P_2 has a relatively small value, the evolution process of the MNSs depends primarily on the adiabatic index for $\rho > 10^{15}$ g/cm^3 (i.e., Γ_3).

(ii) For the EOSs such as ALF2 and H4 for which P_2 has a fairly large value, the evolution

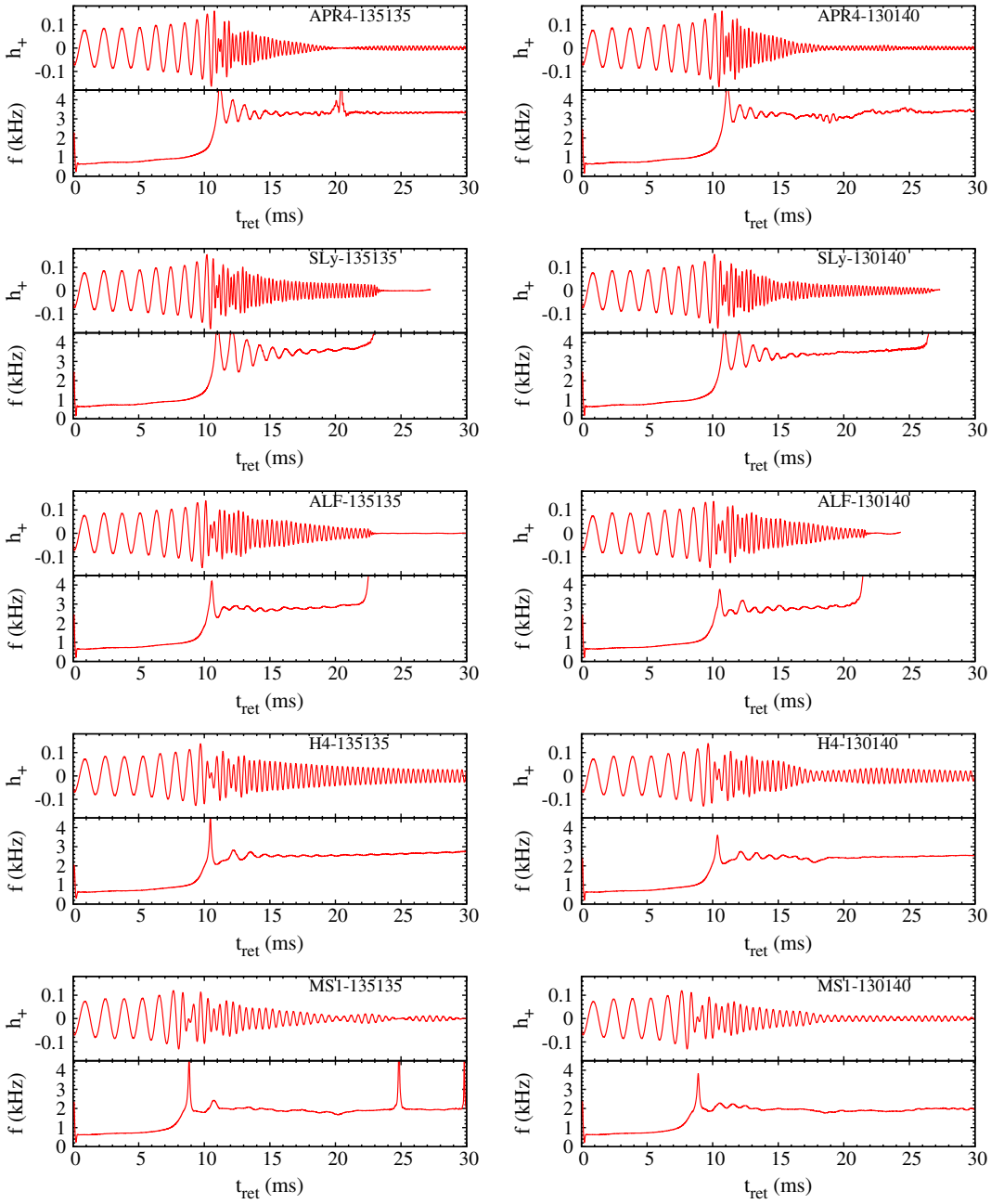

FIG. 7 (color online). Gravitational waves ($h_+ D/m$) and the frequency of gravitational waves f (kHz) as functions of retarded time for models $m_1 = m_2 = 1.35 M_\odot$ and $(m_1, m_2) = (1.30 M_\odot, 1.40 M_\odot)$ with APR4 (top row), SLy (second row), ALF2 (third row), H4 (fourth row), and MS1 (bottom row). For SLy and ALF2, a black hole is eventually formed for $t_{\rm ret} < 30$ ms. For all the models, $\Gamma_{\rm th} = 1.8$. The vertical axis of the gravitational waveforms shows the nondimensional amplitude $h_+ D/m$, with D being the distance to the source. Spikes in the curves of $f(t)$ (for the plot of APR4-135135 and MS1-135135) are not physical; these are generated when the gravitational-wave amplitude is too low to determine the frequency accurately.

process of the MNSs depends on the adiabatic index for $\rho \gtrsim 5 \times 10^{14}$ g/cm^3 (i.e., both on Γ_2 and Γ_3).

(iii) For the stiff EOSs such as MS1 and Shen for which P_2 has a large value, the evolution process of the MNSs depends only on the adiabatic index for $\rho \lesssim 10^{15}$ g/cm^3 (i.e., Γ_2).

Therefore, future gravitational-wave observation for MNSs will be used for exploring the properties of the EOS in a specific density range.

B. Characteristic time scales

As their lifetime is tabulated in one of the columns of Table II, HMNSs collapse to a black hole for several

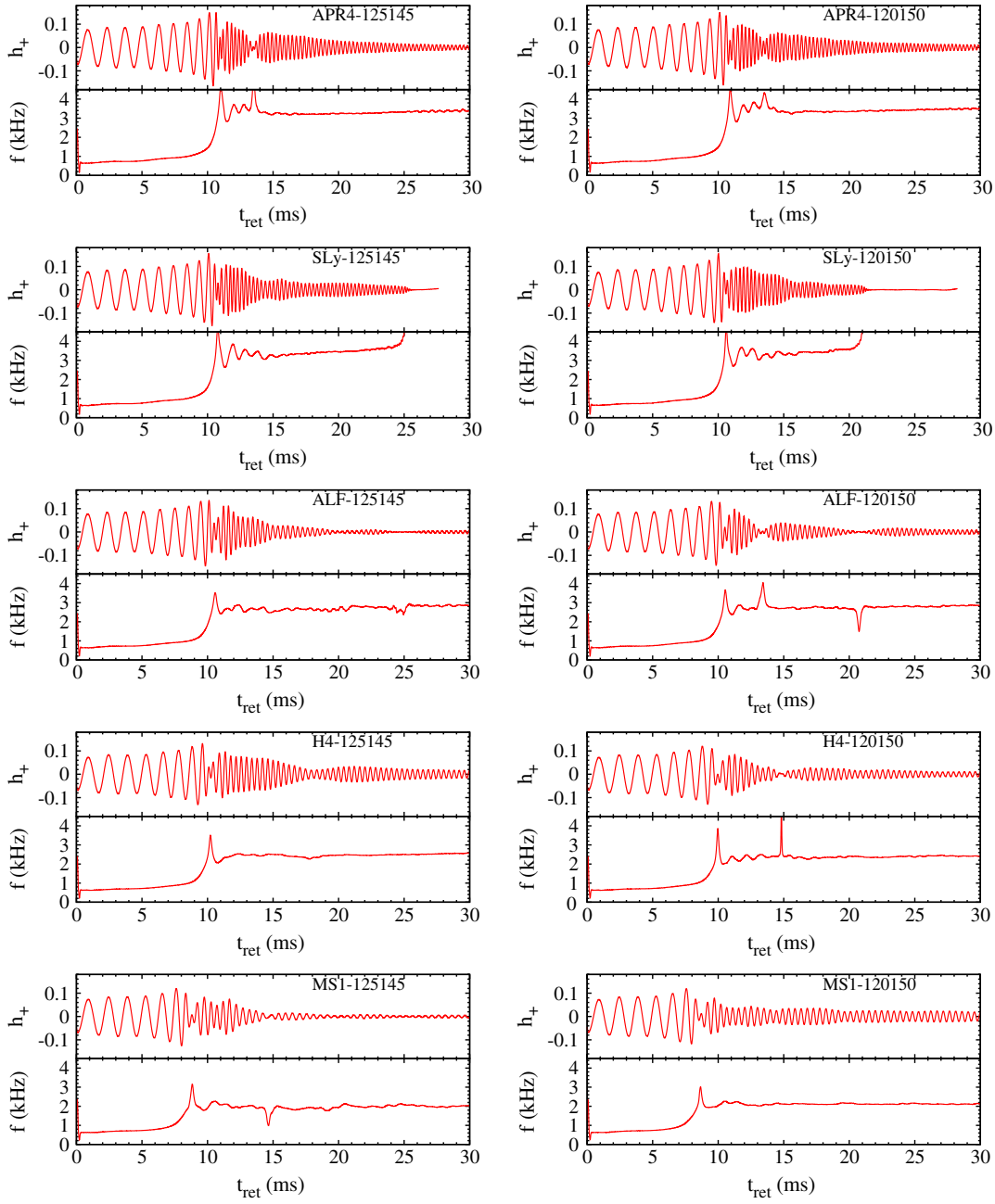

FIG. 8 (color online). The same as Fig. 7 but for $(m_1, m_2) = (1.25M_\odot, 1.45M_\odot)$ (left) and $(1.20M_\odot, 1.50M_\odot)$ (right).

relatively massive models. This collapse is triggered by the angular-momentum loss by the gravitational-wave emission and by the angular-momentum transport process from the inner region of the HMNS to its outer envelope. The transport process can work because the HMNS formed has a nonaxisymmetric structure and exerts the torque to the envelope surrounding it, as already mentioned in Sec. II C. We note that the mass of the disk surrounding the remnant black hole formed after the collapse of the HMNS is in general larger for the longer lifetime of the HMNS for a given EOS (see Table II). In addition, the emissivity of gravitational waves is quite low for not-young HMNS as shown in Sec. IV: This is because the degree of the nonaxisymmetry for the HMNS decreases with time. These facts obviously show that the hydrodynamical angular-momentum transport process plays an essential role for the black-hole formation. Therefore, for the HMNS of lifetime $\sim$10–50 ms, we conclude that the black-hole formation is determined primarily by the hydrodynamical angular-momentum transport process, and write the time scale as $\tau_{\rm hyd}$.

On the other hand, for less-massive HMNSs and SMNSs, neither the emission of gravitational waves nor the hydrodynamical effect are likely to determine their

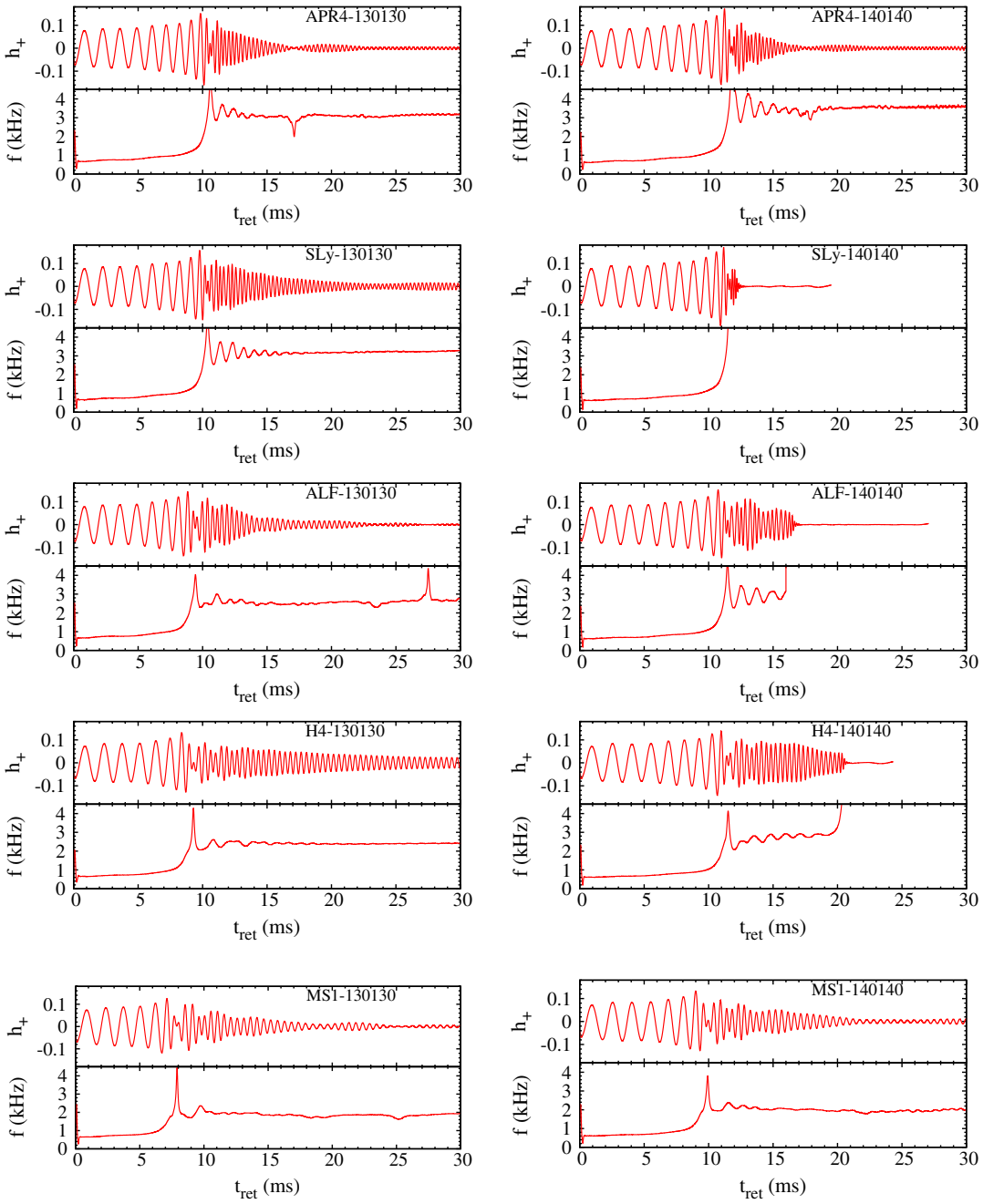

FIG. 9 (color online). The same as Fig. 7 but for $m_1 = m_2 = 1.3M_\odot$ (left) and $m_1 = m_2 = 1.4M_\odot$ (right).

lifetime. For such systems, other dissipation processes (which are not taken into account in our numerical simulations) will play an important role, and the evolution proceeds with the dissipation time scale. If the system is hypermassive and its degree of differential rotation is sufficiently high, the angular-momentum transport process via magnetohydrodynamics effects could trigger the eventual collapse of the HMNS to a black hole (e.g., [40]) with a relatively short time scale $\tau_{\rm wind}$ or $\tau_{\rm mri} \sim 100$ ms or less, which is comparable to $\tau_{\rm hyd}$. If the degree of differential rotation is not high and the thermal effect plays an important role for sustaining the self-gravity of the HMNS, neutrino cooling will play a dominant role for determining the process toward the black-hole formation. According to [10,11], the cooling time scale via the neutrino emission is of order of seconds (hereafter denoted by $\tau_{\rm cool}$), and hence, it is much longer than $\tau_{\rm hyd}$. However, if the degree of differential rotation is not high, $\tau_{\rm cool}$ could be shorter than $\tau_{\rm wind}$ and $\tau_{\rm mri}$. Furthermore, if the remnant mass is smaller than $M_{\rm max,s}(T > 0)$, the magnetic winding and MRI would not trigger the collapse to a black hole. For such a system, the neutrino cooling will trigger the collapse

eventually. Our previous work [10] suggests that this is likely to be the case.

For a smaller-mass system with $M_{\rm max} \lesssim m \lesssim M_{\rm max,s}$, the remnant neutron star is not hypermassive, and it evolves simply to a cold SMNS in $\tau_{\rm cool}$. The cold SMNS will collapse eventually to a black hole after its angular momentum is dissipated by some process such as magnetic dipole radiation. For an even smaller-mass system with $m \lesssim M_{\rm max}$, the remnant neutron star is not supramassive, and it evolves simply to a cold neutron star in $\tau_{\rm cool}$. This is the case for MS1 with $m \lesssim 2.8 M_\odot$.

We may classify the remnant MNSs by its evolution time scale. Figure 6 shows such a classification. In this figure, $\tau_{\rm dyn}$ shows that a black hole is formed in the dynamical time scale after the onset of the merger; $\tau_{\rm hyd}$ shows that a HMNS is formed and its lifetime is determined by the time scale of the hydrodynamical angular-momentum transport (and partly gravitational-wave emission). $\tau_{\rm hyd,s}$ implies that the evolution process is the same as for $\tau_{\rm hyd}$ but the lifetime is shorter than $\sim$10 ms (for this case, the gravitational-wave emission could play an important role for inducing gravitational collapse to a black hole); $\tau_{\rm mag}/\tau_{\rm cool}$ shows that a HMNS is formed and its lifetime, which is longer than $\tau_{\rm hyd}$, would be determined by the time scale of angular-momentum transport by some magneto-hydrodynamics effects or of the neutrino cooling; "SMNS" shows that a SMNS is formed and its lifetime would be much longer than $\tau_{\rm mag}$ and $\tau_{\rm cool}$.

Figure 6 clearly shows that the evolution process and its lifetime of a HMNS depend strongly on its EOS and binary initial mass m. Furthermore, the dependence of the lifetime of a HMNS on the initial mass depends strongly on the EOS. This property is well reflected in the gravitational waveforms, as shown in Sec. IV.

We note that for a given EOS, a disk surrounding a black hole which is formed after the evolution of a HMNS is larger for the *smaller* total mass because of the longer lifetime and the longer angular-momentum transport process. The most popular scenario for the generation of short-hard gamma-ray bursts is that the merger of binary neutron stars produces a system composed of a black hole and a massive disk surrounding it, and the massive disk of high temperature or high magnetic fields subsequently becomes the engine of a gamma-ray burst jet [47]. For more massive disks, the total generated energy of the gamma-ray bursts would be higher. Thus, the total mass of the binary system may be well reflected in the total power of the short-hard gamma-ray bursts. The gravitational-wave observation together with the observation of short gamma-ray bursts could test this hypothesis [48].

Before closing this section, we give a comment on the convergence. In general, for lower grid resolutions, the lifetime of the HMNSs is shorter. The reason inferred is that the lower resolution results in higher numerical dissipation. Hence, the lifetime of the HMNSs found in the numerical result should be considered as the lower limit. For the case that a black hole is formed in a few ms after the onset of the merger, by contrast, the dependence of the lifetime on the grid resolution is quite weak (less than dynamical time scale, $<$1 ms).

C. Dependence of the MNS evolution on binary mass ratio

A MNS formed after the merger is rapidly rotating and nonaxisymmetric (cf. Figs. 4 and 5). Because of this fact, it becomes a strong emitter of gravitational waves. Here, the detailed property of the gravitational waveform depends on the density and velocity profiles of the MNS. The EOS determines the characteristic radius of the MNS, and hence, the frequency of gravitational waves depends strongly on the EOS (see Sec. IV). The merger process depends not only on the EOS but also on the mass ratio and total mass. The mass ratio, in particular, becomes a key ingredient for determining the evolution process of the density profile and the configuration of a MNS in a quasi-stationary state. Through this fact, the mass ratio gives an impact on the gravitational waveforms. In this section, we pay special attention to the dependence for the evolution of the MNS configuration on the binary mass ratio.

First, we summarize the evolution process of MNSs for the equal-mass case (see Fig. 4). For this case, a dumbbell-shaped MNS composed of two cores is formed soon after the onset of the merger irrespective of the EOSs employed. Then, due to the loss of their angular momentum by the hydrodynamical angular-momentum transport and gravitational-wave emission, the shape changes gradually to an ellipsoidal one, and the ellipticity decreases with time. Here, the time scale of the angular-momentum loss depends on the EOS. For APR4 and SLy for which a quasiradial oscillation violently occurs in the early evolution stage of the MNS (see Fig. 3), the time scale of the angular-momentum loss is short ($\sim$ 10 ms), while for H4, MS1, and Shen, the time scale is rather long. For these EOSs, the evolution time scale of MNSs from the dumbbell-like to the spheroidal shape is relatively long, $>$10 ms. These facts can be found from Fig. 4, and also Fig. 4 of [10].

For the unequal-mass case, the evolution process of the MNS configuration is different from that for the equal-mass case. To make the difference clear, we focus here on the case of $m_1 = 1.2 M_\odot$ and $m_2 = 1.5 M_\odot$ (see Fig. 5). For this case, the configuration of the MNS changes with the dynamical time scale in the early evolution stage. The reason is as follows: In the merger stage, the less-massive neutron star is tidally deformed and its outer part is stripped during the merger. Then, the stripped material forms an envelope of the remnant MNS while the core of the less-massive neutron star interacts with the core of the massive companion, and the MNS is composed of two asymmetric cores (see the first two panels of the top row

of Fig. 5). Because the gravity of the less-massive core is much weaker than that of the massive one, it behaves as a satellite that is significantly and dynamically deformed by the main core, varying its configuration with time like an amoeba. During its evolution, the satellite is significantly elongated, encompassing the main core. For such a case, the shape of the MNS (composed of the main core and elongated satellite) becomes approximately spheroidal at a moment (see the third panel of the top row of Fig. 5). For such a moment, the emission of gravitational waves is suppressed transiently (see Sec. IV).

However, after a substantial hydrodynamical angular-momentum transport process which occurs via the interaction with the envelope, the MNS relaxes to a quasistationary state irrespective of the EOSs employed. The quasistationary MNS appears to be composed of major and minor cores which are rotating in a quasistationary manner (see the late-time snapshots of Fig. 5). This system looks like a hammer thrower rotating with a hammer (here the thrower is the major core and the hammer is the minor core). This system subsequently loses the angular momentum primarily through the hydrodynamical angular-momentum transport process, and thus, the degrees of asymmetry decrease gradually, although the time scale of this change is much longer than the dynamical time scale.

All these evolution processes of the MNSs are well reflected in their gravitational waveforms. In the next section, we will summarize the properties of the gravitational waveforms.

IV. GRAVITATIONAL WAVES FROM MNS

Gravitational waves are extracted by calculating the outgoing part of the complex Weyl scalar Ψ_4 at finite coordinate radii $r = 200$–$400M_\odot$ and by integrating Ψ_4 twice in time (see, e.g., [49] for our method). In this work, we focus only on $(l, m) = (2, 2)$ modes, which dominate over the gravitational-wave amplitude during the MNS phase.

Figures 7–11 display the plus mode of gravitational waves h_+ and the corresponding frequencies of gravitational waves emitted by MNSs for a variety of EOSs and binary masses. Here, gravitational waves shown are those observed along the rotational axis which is perpendicular to the binary orbital plane, and defined by $h_+ D/m$ where D is the distance from the source. The frequency is determined by the change rate of the phase of $h := h_+ - ih_\times$, with $h_\times$ being the cross mode of gravitational waves. In this work, we evaluate the frequency by calculating $\Psi_4/\int \Psi_4 dt$ as employed in Ref. [36]. Figures 7 and 8 display gravitational waves for $m = 2.7M_\odot$ with four mass

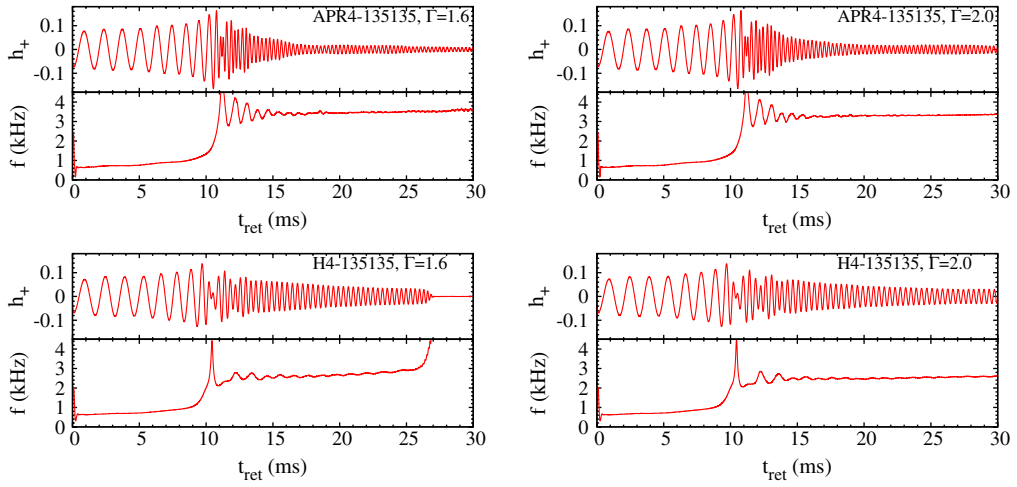

FIG. 10 (color online). The same as Fig. 7 but for $m_1 = m_2 = 1.35M_\odot$ and $\Gamma_{\rm th} = 1.6$ (left) and 2.0 (right) with APR4 (upper row) and H4 (lower row) EOSs.

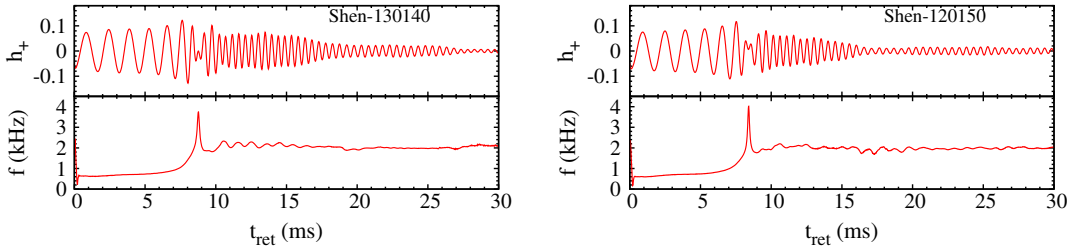

FIG. 11 (color online). The same as Fig. 7 but for Shen EOSs with $(m_1, m_2) = (1.3M_\odot, 1.4M_\odot)$ and $(1.2M_\odot, 1.5M_\odot)$.

ratios and five piecewise polytropic EOSs (APR, SLy, ALF2, H4, and MS1). Figure 9 displays gravitational waves for the equal-mass models with $m = 2.6M_\odot$ and $2.8M_\odot$ with five piecewise polytropic EOSs. Figure 10 displays gravitational waves for $m_1 = m_2 = 1.35M_\odot$ with APR4 and H4 EOSs and with $\Gamma_{\rm th} = 1.6$ and 2.0. Figure 11 displays gravitational waves for Shen EOSs with $(m_1, m_2) = (1.3M_\odot, 1.4M_\odot)$ and $(1.2M_\odot, 1.5M_\odot)$. Gravitational waves for Shen EOS are also shown in Fig. 4 of [10] for the equal-mass models, to which the reader may refer: For this EOS, the gravitational waveforms are qualitatively similar to those for H4.

Gravitational waves emitted by MNSs are characterized by their quasiperiodic nature. Namely, the frequency of gravitational waves remains approximately constant for more than 10 wave cycles. Nevertheless, the frequency of gravitational waves is not totally constant and changes with time. Furthermore, the characteristic frequency and the time-variation feature of the frequency and amplitude depend strongly on the EOS, total mass, and mass ratio of the binary system. In the following, we summarize the features of gravitational waves emitted by MNSs in more detail.

A. Amplitude

Broadly speaking, the amplitude of quasiperiodic gravitational waves emitted by MNSs decreases with time because the angular momentum of the MNSs is lost by the hydrodynamical angular-momentum transport process and gravitational-wave emission. However, the feature in the time variation depends on the EOS and mass ratio of the binary.

There are two patterns for the damping process of the gravitational-wave amplitude. One is that the amplitude decreases approximately monotonically with time (besides small modulation), and the damping time scale increases with time. This is the case for the equal-mass model for all the piecewise polytropic EOSs, APR4, SLy, ALF2, H4, and MS1, irrespective of the value of $\Gamma_{\rm th}$ and total mass, as well as for Shen (see Figs. 7, 9, and 10 as well as Fig. 4 of [10]). For APR4 and SLy, an oscillating MNS of nonaxisymmetric shape (dumbbell-like or ellipsoidal) is formed and quickly loses its angular momentum by the hydrodynamical angular-momentum transport and gravitational-wave emission. The damping time scale of the nonaxisymmetric degree (and hence the gravitational-wave amplitude) is short, $\sim$10 ms, during the stage that the quasiradial oscillation amplitude of the MNS is high. Subsequently, the MNS settles to a weakly deformed quasistationary ellipsoid, and then the gravitational-wave amplitude relaxes approximately to a small constant. For H4, MS1, and Shen, by contrast, the damping time scale of the gravitational-wave amplitude is relatively long for the entire evolution stage of the MNSs. This seems to be due to the fact that the angular-momentum transport process from the MNS to the surrounding envelope is not as efficient as in the APR4 and SLy cases. The probable reason for this is that the radial oscillation amplitude of the MNSs is low for these stiff EOSs, and thus, a quasistationary nonaxisymmetric MNS is formed in a short time scale (a few ms) after the onset of the merger. Namely, the merger proceeds relatively in a mild way, resulting in a long-term angular-momentum transport process. Figures 9 and 10 show that this fact holds irrespective of the total mass and the value of $\Gamma_{\rm th}$. For ALF2, the efficiency of the angular-momentum transport is lower than for APR4 and SLy but higher than for H4, MS1, and Shen. Thus, the damping time scale of gravitational-wave amplitude is between two cases.

One point to be noted is that the gravitational-wave amplitude for the late stage (for $t - t_{\rm merge} \gtrsim 10$ ms where $t_{\rm merge}$ denotes the time for the onset of the merger) remains high for H4 and Shen. This seems to reflect the difference in the adiabatic index of the high-density range; for these EOSs, the central region of the MNS has low values of Γ_2 and Γ_3 (see also Fig. 1). With such relatively small values, we found that a dumbbell-like structure rather than the ellipsoidal structure is preserved for the MNS, and hence, the gravitational-wave amplitude is enhanced.

The second pattern is that the gravitational-wave amplitude damps with a characteristic modulation. This pattern is often found for unequal-mass models, in particular for $q = 0.8$ (see Fig. 8). The origin of this modulation is explained as follows: During the early stage of the MNS evolution, its central region appears to be composed of a massive core and a deformed satellite for which the shape varies in the early stage of the evolution (cf. Sec. III C). Here, the massive core and satellite come from the massive and less-massive neutron stars of the binary, respectively. In the early stage of the MNSs, two asymmetric cores rotate around each other, and high-amplitude quasiperiodic gravitational waves are emitted for $\sim$3–5 ms. Then, the amplitude once damps to be very small at a moment and subsequently, long-term quasiperiodic gravitational waves are again emitted. This feature is clearly seen for APR4-120150, APR4-125145, ALF2-120150, and H4-120150. The mechanism for producing this pattern is closely related to the evolution process of the MNSs (see Sec. III C). For these asymmetric merger cases, asymmetric double cores are formed as already mentioned. However, the less-massive core dynamically changes its shape (like amoeba), and at the moment that the gravitational-wave amplitude is small, the less-massive core has a highly deformed shape surrounding the massive core. Namely, at this moment, not double cores but a single nearly spheroidal core is formed (see the third panel of Fig. 5). However, after this moment, an asymmetric double-core structure is formed again (like a hammer-thrower shape). Because the resulting double-core structure is highly nonaxisymmetric, quasiperiodic gravitational waves with high amplitude are emitted.

For MS1-120150 and Shen-120150, the MNS also has an asymmetric double-core structure which is alive for a

long time scale $\gg 10$ ms. In this case, the MNS never has the moment at which a spheroidal shape is realized, and hence, the gravitational-wave amplitude is stably high, although a modulation in the amplitude is still observed.

B. Frequency

As already mentioned, the frequency of gravitational waves emitted by MNSs is approximately constant (see Figs. 7–11). The exception to this occurs for some models in the very early stage just after the formation of some of the MNSs in which the frequency oscillates with a dynamical time scale (this can be observed for all the models to a greater or lesser degree) or for the stage just before the formation of a black hole in which the frequency increases steeply with time (see, e.g., the results for models SLy-135135, SLy-120150, ALF2-135135, ALF2-130140, ALF2-140140, H4-135135, and H4-140140). These qualitative features hold irrespective of the EOSs.

Figure 12 plots the Fourier spectra for some of gravitational waves displayed in Figs. 7–11. Here, we plot the effective amplitude defined by $|h(f)f|$ as a function of f where $h(f)$ is the Fourier spectrum of $h_+ - ih_\times$. This shows that there are indeed characteristic frequencies ~ 2 kHz $\lesssim f \lesssim 4$ kHz, at which the spectrum amplitude

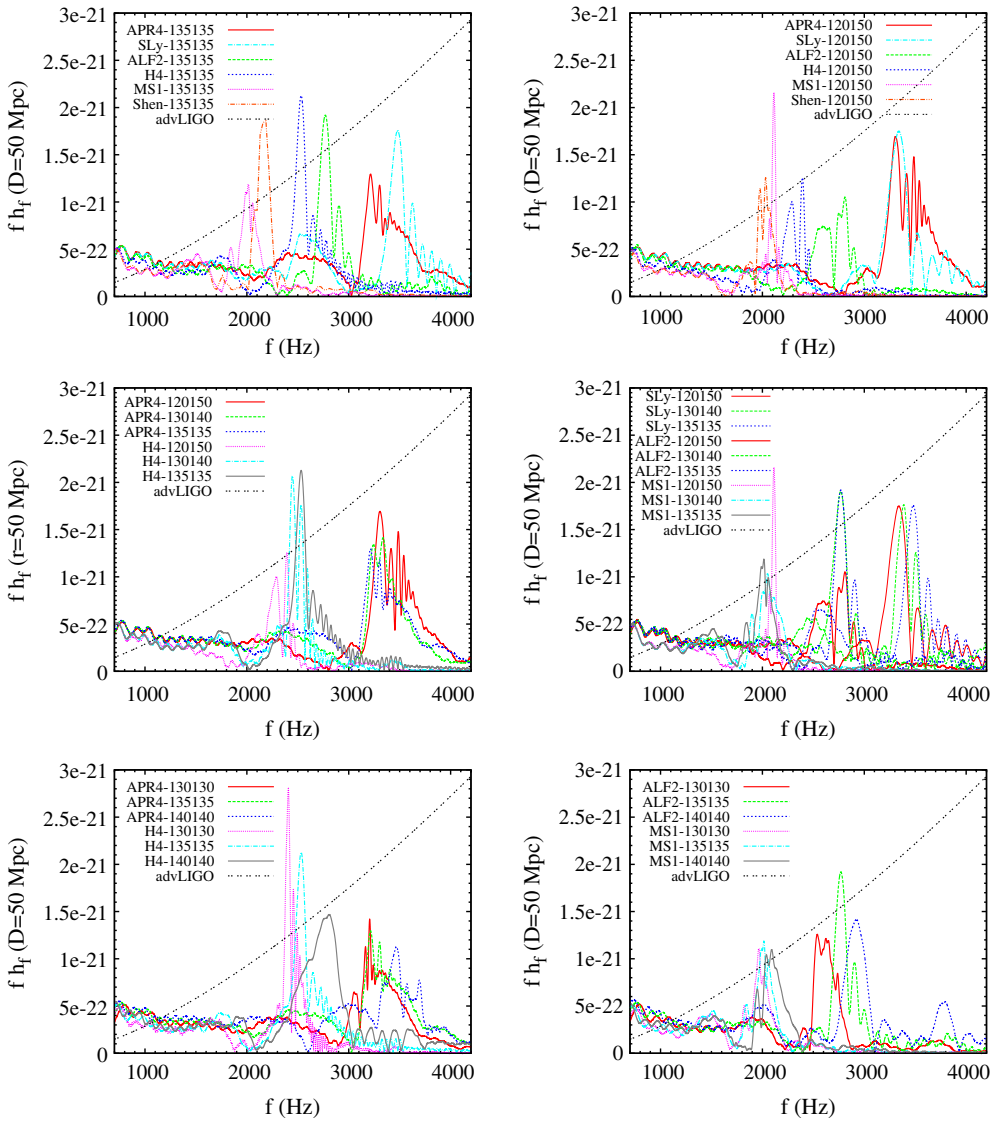

FIG. 12 (color online). Fourier spectra of gravitational waves for some of the results shown in Figs. 7–11. Top left: For $m_1 = m_2 = 1.35M_\odot$ with $\Gamma_{\rm th} = 1.8$ and with five piecewise polytropic and Shen EOSs. Top right: The same as top left but for $m_1 = 1.2M_\odot$ and $m_2 = 1.5M_\odot$. Middle left: For three mass ratios with $m = 2.7M_\odot$, $\Gamma_{\rm th} = 1.8$, and with APR4 and H4. Middle right: The same as middle left but for SLy, ALF2, and MS1. Bottom left: For equal-mass models with $m = 2.6$, 2.7, and $2.8M_\odot$, $\Gamma_{\rm th} = 1.8$, and with APR4 and H4. Bottom right: The same as bottom left but for ALF2 and MS1. The amplitude is shown for the hypothetical event at a distance of $D = 50$ Mpc along the direction perpendicular to the orbital plane (the most optimistic direction). The black dot-dotted curve is the noise spectrum of the advanced LIGO with an optimistic configuration for the detection of high-frequency gravitational waves (see Ref. [56]).

TABLE III. Characteristic frequencies of gravitational waves emitted by MNSs which are determined by two different methods: Fourier peak denotes the peak frequencies of the effective amplitude $h(f)f$. $f_{\rm ave,5ms}$, $f_{\rm ave,10ms}$, and $f_{\rm ave,20ms}$ denote the results for Eq. (11) with 5, 10, and 20 ms time integration after the formation of the MNSs; the — denotes that the lifetime of MNSs is shorter than the corresponding integration time. The deviation of $f_{\rm ave}$ shown here denotes σ_f. The multiple values shown for the Fourier peak imply that we found many peaks for which their peak values of $h(f)f$ are larger than 80% of its maximum value. $f^{\rm fit}_{\rm ave,10ms}$ denote the averaged frequency calculated from the best-fit results of Eqs. (15)–(17). The last four columns show the maximum values of $\mathcal{M}$ for a fitting procedure with the number of parameters, $N_{\rm p} = 13$, 12, 11, and 10 (see Sec. V).

Model	$\Gamma_{\rm th}$	Fourier peak (kHz)	$f_{\rm ave,5ms}$ (kHz)	$f_{\rm ave,10ms}$ (kHz)	$f_{\rm ave,20ms}$ (kHz)	$f^{\rm fit}_{\rm ave,10ms}$ (kHz)	$\mathcal{M}_{N_{\rm p}=13}$	$\mathcal{M}_{N_{\rm p}=12}$	$\mathcal{M}_{N_{\rm p}=11}$	$\mathcal{M}_{N_{\rm p}=10}$
APR4-130150	1.8	3.40	3.48 ± 0.47	3.46 ± 0.37	3.49 ± 0.33	3.39 ± 0.29	0.910	0.894	0.894	0.883
APR4-140140	1.8	3.47	3.59 ± 0.64	3.57 ± 0.58	3.53 ± 0.44	3.59 ± 0.59	0.968	0.968	0.967	0.965
APR4-120150	1.6	3.31 3.54	3.47 ± 0.30	3.44 ± 0.27	—	3.44 ± 0.24	0.963	0.962	0.959	0.945
APR4-120150	1.8	3.31, 3.43	3.44 ± 0.30	3.41 ± 0.24	3.41 ± 0.21	3.41 ± 0.23	0.959	0.959	0.954	0.951
APR4-120150	2.0	3.18	3.32 ± 0.32	3.27 ± 0.26	3.27 ± 0.22	3.16 ± 0.20	0.924	0.924	0.919	0.919
APR4-125145	1.8	3.23	3.36 ± 0.31	3.31 ± 0.25	3.31 ± 0.23	3.20 ± 0.18	0.930	0.930	0.926	0.907
APR4-130140	1.8	3.28, 3.31, 3.40	3.30 ± 0.29	3.27 ± 0.28	3.29 ± 0.26	3.26 ± 0.26	0.982	0.982	0.981	0.968
APR4-135135	1.6	3.45	3.46 ± 0.42	3.45 ± 0.37	3.46 ± 0.30	3.44 ± 0.33	0.970	0.967	0.967	0.942
APR4-135135	1.8	3.21, 3.30	3.31 ± 0.41	3.28 ± 0.37	3.28 ± 0.34	3.27 ± 0.33	0.970	0.969	0.969	0.947
APR4-135135	2.0	3.29, 3.37	3.35 ± 0.39	3.33 ± 0.34	3.33 ± 0.29	3.29 ± 0.17	0.952	0.952	0.947	0.947
APR4-120140	1.8	3.14	3.15 ± 0.21	3.13 ± 0.19	3.12 ± 0.18	3.11 ± 0.16	0.982	0.981	0.981	0.972
APR4-125135	1.8	3.20	3.22 ± 0.25	3.19 ± 0.24	—	3.15 ± 0.17	0.975	0.975	0.974	0.963
APR4-130130	1.8	3.21	3.22 ± 0.28	3.19 ± 0.26	3.18 ± 0.24	3.18 ± 0.28	0.974	0.970	0.965	0.958
SLy-120150	1.8	3.34	3.31 ± 0.26	3.35 ± 0.24	—	3.32 ± 0.19	0.984	0.983	0.979	0.979
SLy-125145	1.8	3.32	3.29 ± 0.32	3.32 ± 0.27	—	3.31 ± 0.28	0.969	0.957	0.948	0.948
SLy-130140	1.8	3.39	3.35 ± 0.47	3.36 ± 0.40	—	3.38 ± 0.42	0.965	0.959	0.958	0.913
SLy-135135	1.8	3.48	3.41 ± 0.58	3.46 ± 0.48	—	3.47 ± 0.47	0.963	0.952	0.946	0.893
SLy-130130	1.8	3.16	3.17 ± 0.34	3.16 ± 0.29	3.18 ± 0.26	3.16 ± 0.28	0.988	0.988	0.987	0.972
ALF2-140140	1.8	2.92	2.93 ± 0.42	—	—	2.90 ± 0.34	0.980	0.955	0.952	0.911
ALF2-120150	1.8	2.74, 2.82, 2.87	2.70 ± 0.19	2.71 ± 0.16	2.73 ± 0.15	2.61 ± 0.20	0.924	0.916	0.916	0.907
ALF2-125145	1.8	2.65	2.66 ± 0.14	2.66 ± 0.13	2.67 ± 0.13	2.63 ± 0.09	0.985	0.985	0.985	0.985
ALF2-130140	1.8	2.77	2.73 ± 0.19	2.75 ± 0.17	—	2.75 ± 0.12	0.981	0.979	0.978	0.977
ALF2-135135	1.8	2.77	2.74 ± 0.17	2.76 ± 0.15	—	2.74 ± 0.12	0.989	0.989	0.981	0.981
ALF2-130130	1.8	2.54, 2.63, 2.65	2.58 ± 0.18	2.56 ± 0.16	2.56 ± 0.15	2.55 ± 0.12	0.978	0.975	0.973	0.972
H4-130160	1.8	2.72	2.64 ± 0.26	—	—	2.64 ± 0.26	0.973	0.965	0.963	0.942
H4-145145	1.8	2.90, 2.96	2.97 ± 0.56	—	—	2.93 ± 0.49	0.965	0.965	0.942	0.941
H4-130150	1.8	2.45, 2.56	2.44 ± 0.17	2.45 ± 0.15	2.54 ± 0.17	2.42 ± 0.09	0.958	0.956	0.956	0.952
H4-140140	1.8	2.75, 2.81	2.63 ± 0.23	2.77 ± 0.41	—	2.69 ± 0.22	0.975	0.975	0.966	0.951
H4-120150	1.6	2.22, 2.32, 2.38	2.28 ± 0.16	2.29 ± 0.14	2.31 ± 0.14	2.30 ± 0.03	0.980	0.977	0.977	0.966
H4-120150	1.8	2.29, 2.39	2.30 ± 0.18	2.31 ± 0.15	2.33 ± 0.14	2.28 ± 0.09	0.955	0.955	0.955	0.939
H4-120150	2.0	2.30	2.24 ± 0.15	2.22 ± 0.14	2.26 ± 0.12	2.22 ± 0.08	0.983	0.980	0.980	0.973
H4-125145	1.8	2.44	2.41 ± 0.15	2.41 ± 0.13	2.44 ± 0.11	2.39 ± 0.13	0.981	0.981	0.980	0.980
H4-130140	1.8	2.43, 2.52	2.42 ± 0.17	2.42 ± 0.15	2.44 ± 0.13	2.40 ± 0.13	0.968	0.968	0.967	0.966
H4-135135	1.6	2.59	2.49 ± 0.19	2.54 ± 0.16	—	2.54 ± 0.15	0.985	0.968	0.966	0.960
H4-135135	1.8	2.53	2.44 ± 0.20	2.48 ± 0.16	2.54 ± 0.17	2.48 ± 0.14	0.984	0.982	0.978	0.963
H4-135135	2.0	2.49	2.39 ± 0.21	2.43 ± 0.17	2.47 ± 0.15	2.44 ± 0.14	0.977	0.977	0.972	0.972
H4-120140	1.8	2.34, 2.37, 2.43	2.30 ± 0.15	2.30 ± 0.14	2.33 ± 0.13	2.32 ± 0.06	0.948	0.948	0.947	0.912
H4-125135	1.8	2.26	2.29 ± 0.17	2.27 ± 0.14	2.26 ± 0.12	2.28 ± 0.14	0.973	0.971	0.971	0.966
H4-130130	1.8	2.31	2.35 ± 0.18	2.38 ± 0.14	2.38 ± 0.11	2.37 ± 0.12	0.982	0.982	0.980	0.980
MS1-130160	1.8	2.12	2.07 ± 0.15	2.06 ± 0.13	—	2.02 ± 0.14	0.967	0.967	0.965	0.956
MS1-145145	1.8	2.11	2.12 ± 0.15	2.09 ± 0.13	—	2.09 ± 0.12	0.979	0.979	0.978	0.978
MS1-140140	1.8	2.04, 2.09	2.09 ± 0.14	2.07 ± 0.12	2.05 ± 0.12	2.06 ± 0.12	0.972	0.972	0.968	0.964
MS1-120150	1.8	2.11	2.08 ± 0.11	2.09 ± 0.09	2.10 ± 0.07	2.08 ± 0.10	0.987	0.987	0.987	0.983
MS1-125145	1.8	2.02, 2.08	2.02 ± 0.14	1.99 ± 0.15	1.99 ± 0.14	1.97 ± 0.16	0.959	0.959	0.955	0.953
MS1-130140	1.8	2.05	2.06 ± 0.14	2.02 ± 0.13	2.00 ± 0.13	2.03 ± 0.11	0.978	0.976	0.975	0.973
MS1-135135	1.8	1.99, 2.02, 2.05	1.98 ± 0.17	1.96 ± 0.15	1.95 ± 0.14	2.00 ± 0.22	0.951	0.951	0.941	0.935
MS1-130130	1.8	1.96	1.94 ± 0.18	1.93 ± 0.15	1.91 ± 0.15	1.96 ± 0.22	0.950	0.950	0.948	0.943
Shen-120150	—	1.97, 2.03	2.02 ± 0.15	2.00 ± 0.13	2.00 ± 0.12	2.01 ± 0.07	0.985	0.977	0.977	0.977

TABLE III. (*Continued*)

Model	$\Gamma_{\rm th}$	Fourier peak (kHz)	$f_{\rm ave,5ms}$ (kHz)	$f_{\rm ave,10ms}$ (kHz)	$f_{\rm ave,20ms}$ (kHz)	$f^{\rm fit}_{\rm ave,10ms}$ (kHz)	$\mathcal{M}_{N_{\rm p}=13}$	$\mathcal{M}_{N_{\rm p}=12}$	$\mathcal{M}_{N_{\rm p}=11}$	$\mathcal{M}_{N_{\rm p}=10}$
Shen-125145	—	2.10, 2.18	2.15 ± 0.17	2.17 ± 0.15	2.15 ± 0.13	2.16 ± 0.12	0.972	0.966	0.964	0.963
Shen-130140	—	2.09, 2.12	2.08 ± 0.18	2.09 ± 0.14	2.06 ± 0.15	2.07 ± 0.14	0.972	0.971	0.971	0.967
Shen-135135	—	2.18	2.18 ± 0.18	2.23 ± 0.14	2.21 ± 0.11	2.27 ± 0.06	0.971	0.969	0.967	0.967
Shen-140140	—	2.28	2.29 ± 0.26	2.28 ± 0.19	2.27 ± 0.16	2.31 ± 0.05	0.989	0.989	0.989	0.989
Shen-150150	—	2.29	2.22 ± 0.24	2.13 ± 0.18	2.11 ± 0.16	2.25 ± 0.12	0.989	0.989	0.989	0.984
Shen-160160	—	2.49	2.38 ± 0.37	2.51 ± 0.50	—	2.49 ± 0.20	0.943	0.943	0.930	0.919

is high, irrespective of models (see also Table III for the frequency of the spectrum peak). For a "soft" EOS that yields a compact neutron star for the canonical mass (i.e., APR4, SLy, and ALF2 in this paper), the characteristic frequency is higher with $f \gtrsim 3$ kHz, while for other "stiff" EOSs that yield a large-radius neutron $R \gtrsim 13$ km, it is lower typically as $f \sim 2$–2.5 kHz. The reason for this property is explained as follows: The spin angular velocity of the MNSs is close to the Kepler velocity, and hence, the characteristic frequencies of gravitational waves are qualitatively proportional to $(M_{\rm MNS}/R^3_{\rm MNS})^{1/2}$ where $M_{\rm MNS}$ and $R_{\rm MNS}$ denote the typical mass and radius of a MNS. Here, the value of $R_{\rm MNS}$ should be approximately proportional to the radius of neutron stars of the canonical mass, and hence, it is reflected in the characteristic frequency. It should also be mentioned that the characteristic frequency depends on the value of $\Gamma_{\rm th}$: For the smaller value of it, the frequency is slightly higher for many cases, because the effect of shock heating is weaker, and the MNS becomes more compact.

As pointed out in [23], we also find that a certain correlation exists between the characteristic frequency and a stellar radius of a cold spherical neutron star in isolation. Figure 13 plots the frequency of the Fourier spectrum peak as a function of the neutron star radius of mass $1.8M_\odot$ (upper panels) and $1.6M_\odot$ (lower panels) for a given EOS (denoted by $R_{1.8}$ and $R_{1.6}$ in units of km) for $m = 2.7M_\odot$ (left panels) and $2.6M_\odot$ (right panels) [50]. For the $m = 2.7M_\odot$ case, we also plot the Fourier spectrum peak of the results of [23] for comparison [52]. The dotted curves are

$$f = (4.0 \pm 0.3)\ {\rm kHz}\left(\frac{(R_{1.8}/{\rm km}) - 2}{8}\right)^{-3/2} \quad (7)$$

for the upper left panel,

$$f = (3.85 \pm 0.15)\ {\rm kHz}\left(\frac{(R_{1.8}/{\rm km}) - 2}{8}\right)^{-3/2} \quad (8)$$

for the upper right panel,

$$f = (4.15 \pm 0.35)\ {\rm kHz}\left(\frac{(R_{1.6}/{\rm km}) - 2}{8}\right)^{-3/2} \quad (9)$$

for the lower left panel, and

$$f = (3.95 \pm 0.25)\ {\rm kHz}\left(\frac{(R_{1.6}/{\rm km}) - 2}{8}\right)^{-3/2} \quad (10)$$

for the lower right panel. These curves approximately show the upper and lower limits of the characteristic frequency. We note that the subtraction factor of -2 for $R_{1.8}$ and $R_{1.6}$ is empirically needed to capture the upper and lower limits for the star of radius ~ 11 km. The reason seems to be due to the fact that general relativistic corrections play an important role for the small value of the neutron star radius. The reason why $R_{1.8}$ is employed is that we found it a better choice to get a clear correlation between the peak frequency and a neutron star radius for our results. The choice of $R_{1.6}$ is done following [23]. In both cases, our results of the correlation between the characteristic frequency and a stellar radius are largely consistent with the results of [23] within the uncertainty represented with the dotted curves.

For the figure, we plotted all the values of the peak frequency when we found multiple peaks; for some models, we plotted 2 or 3 points. We also plotted all the data irrespective of the values of $\Gamma_{\rm th}$ for APR4 and H4: Possible unknown dispersion associated with the shock heating effect is taken into account in these plots. Nevertheless, we still find a fairly clear correlation for the choice of $R_{1.8}$. In particular for the lower-mass models ($m = 2.6M_\odot$), the dispersion is quite small. This figure suggests that if we can determine the peak frequency accurately, we will be able to constrain the radius of the neutron star with the uncertainty of ~ 1 km. However, it is also found that it is not easy to reduce the estimation error to $\ll 1$ km, because of the presence of the systematic dispersion of the peak frequency.

The peak frequencies are associated with the major frequencies of the quasiperiodic oscillation of gravitational waves emitted by the MNSs as found in Figs. 7–11. However, as already mentioned, the (nonaxisymmetric) oscillation frequency of the MNSs changes during the evolution due to a quasiradial oscillation (which changes the peak frequency as $R^{-3/2}_{\rm MNS}$) and to the secular dissipation processes of their angular momentum, and hence, the major frequencies change with time, resulting in the broadening of the peak or appearance of the multiple peaks (e.g., the spectra for APR4-135135, APR4-130140, H4-120150, ALF2-130130, and ALF2-120150). This broadening is not very large for particular models such as equal-mass models

of some EOSs (see a discussion in the last paragraph of this section), and thus, for these particular cases, the characteristic frequency may be determined with a small dispersion. However, in general, the broadening value is ~10% of the peak frequencies which is ~2–3.5 kHz. Therefore, it will not be easy to strictly determine the peak frequencies from the Fourier spectrum. This situation will bring a serious problem in the real data analysis, in which the noise level is by several 10% as large as the signal amplitude; the peak will not be determined strictly due to the presence of many fake peaks and spurious broadening.

To estimate the possible magnitude of the broadening, we also determine the average frequency from the results of the frequency f by [12]

$$f_{\rm ave} := \frac{\int f|h|dt}{\int |h|dt}, \tag{11}$$

where we used $|h| = (h_+^2 + h_\times^2)^{1/2}$ as the weight factor. Then, we define the physical deviation of the major frequency by

$$\sigma_f^2 := \frac{\int (f - f_{\rm ave})^2 |h| dt}{\int |h| dt}. \tag{12}$$

Here, the time integration is performed for 5, 10, and 20 ms after the formation of the MNSs, because for each time segment, the frequencies are changed. Table III lists the average frequency and the deviation determined for 5, 10, and 20 ms integration.

Table III as well as Fig. 12 shows that the values of $f_{\rm ave}$ agree approximately with the peak frequency of the Fourier spectrum irrespective of the integration time. However, as expected, the value of $f_{\rm ave}$ changes with time. It is also found that the magnitude of the deviation σ_f is not negligible. For APR4 and SLy, for which the neutron star radius is rather small and the amplitude of a quasiradial oscillation induced at the formation of the MNSs is rather large, the magnitude of the deviation is 0.3–0.4 kHz. This indicates that for determining the peak frequency from the Fourier spectrum, the uncertainty of this magnitude has to be kept in mind. For other EOSs, the deviation is relatively small. However, it is still 0.1–0.2 kHz. To summarize, we conclude that the characteristic frequency of gravitational waves emitted by the MNSs changes with time in general, and such time variation is the major source of the broadening of the peak frequency found in Fig. 13.

There is also an uncertainty due to the grid resolution of the simulation. The averaged value of the frequency converges within ~0.1 kHz error. This error causes an uncertainty of the correlations between the Fourier peak and the radius of a neutron stars with an error about 0.1 km. However, the half width of Fourier peaks, which is about σ_f, is larger than the uncertainty due to the grid resolution. Thus we consider that an uncertainty ~0.1 kHz is not quite significant.

Before closing this section, we summarize several interesting properties found in the Fourier spectrum. The first one is that the peak frequencies vary with the mass ratio

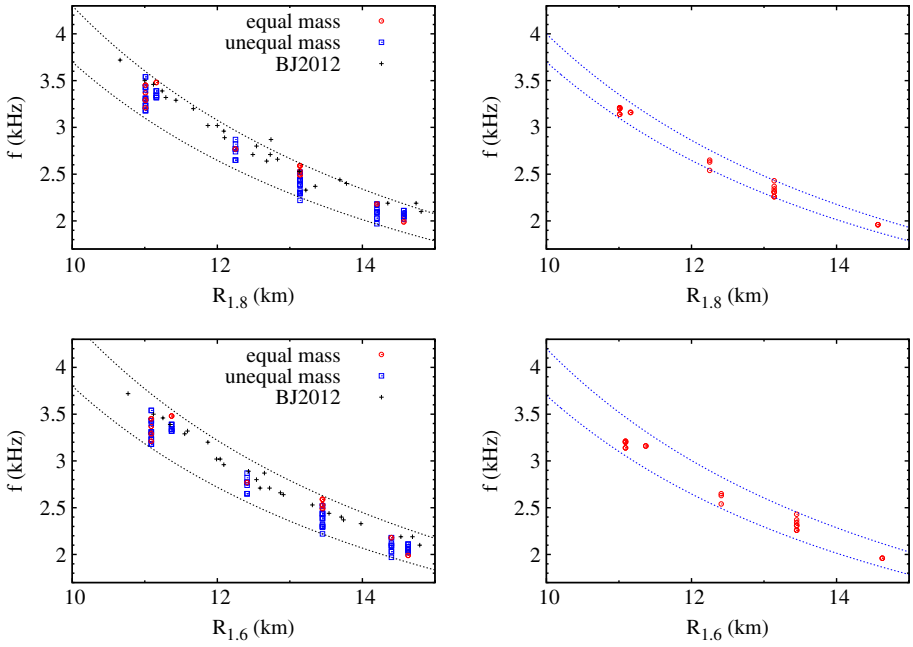

FIG. 13 (color online). The frequency of the Fourier spectrum peak as a function of the neutron star radius of $M = 1.8M_\odot$ (upper panels) and $M = 1.6M_\odot$ (lower panels) with a given EOS for $m = 2.7M_\odot$ (left panels) and $2.6M_\odot$ (right panels). In the right panels, we plotted all the data (equal-mass and unequal-mass data) using the same symbol. In the left panels, the cross symbols denote the data of [23].

even for the same total mass m (see Table III) and that the feature of this variation depends on the EOS. For APR4, SLy, and ALF2, the frequency depends only weakly on the mass ratio. For H4 and Shen, the frequency is lower for the lower values of q, i.e., for a more asymmetric system. By contrast, for MS1, the frequency tends to be higher for a more asymmetric system. This property causes a dispersion in the relation between the peak frequency and $R_{1.8}$ displayed in Fig. 13. The second one is that the peak amplitude of the Fourier spectrum decreases with the decrease of q for ALF2, H4, and Shen, while it increases with the decrease of q for APR4 and MS1 (see Fig. 12). In other words, for ALF2, H4, and Shen, the spectrum peak is sharper for the equal-mass binaries, while for APR4 and MS1, it is sharper for the asymmetric binaries. These properties will be used for constraining the EOS if the peak frequencies are determined for a variety of binary neutron star mergers.

V. MODELING GRAVITATIONAL WAVEFORMS FROM MNS

In this section, we attempt to construct a fitting formula of gravitational waveforms from MNSs.

A. Fitting formula

In this section, we describe possible fitting formulas for the waveforms of quasiperiodic gravitational waves emitted by MNSs. There are two conflicting requirements for the fitting formulas:

(i) On the one hand, we want fitting formulas by which various numerical waveforms are well fitted universally. This generally requires more numbers of free parameters.

(ii) On the other hand, we want fitting formulas that are controlled by minimal numbers of free parameters, to minimize the computational costs for the fitting in the parameter survey procedures. In addition, with smaller numbers of free parameters, the risk of unphysical fitting is decreased, and thus, the physical meaning of each parameter in the best-fitted case will be clearer.

Thus, we have to find an optimized fitting formula that is described by an optimized number of parameters. To discover the optimized fitting formula, as a first step, we introduce a formula that reproduces many characteristic properties of numerical waveforms, without caring for the optimization. Then, we search for the way to reduce the number of parameters while keeping the matching degree as high as possible.

The universal features of gravitational waves emitted by MNSs are described in Sec. IV and summarized as follows:

(i) The frequency of gravitational waves reaches a peak soon after the merger sets in (or in other words, in the final moment of the inspiral phase) and then experiences a damping oscillation for several oscillation periods, eventually settling approximately to a constant value, although a long-term secular change associated with the change of the state of MNSs is always present.

(ii) Soon after the onset of the merger, the amplitude of gravitational waves becomes very low. However, subsequently, the amplitude steeply increases, and then it decreases either monotonically or with modulations.

(iii) The damping time scale of the amplitude is of the order of 10 ms for most MNS models although for some EOSs such as H4 and Shen, the damping time scale is much longer than 10 ms.

The fact (iii) implies that the emissivity of gravitational waves by MNSs is in general high for the first $\sim$10 ms after their formation. Hence, to save the search costs, we focus on gravitational waves in this time range, considering the 10 ms-window function

$$W(t) := \begin{cases} 1 & \text{for } t_i \le t \le t_f, \\ 0 & \text{otherwise,} \end{cases} \tag{13}$$

where $t = t_i$ is the time at which the frequency peak is reached and $t_f = t_i + 10$ ms. In the following, we define the origin of the time by setting $t_i = 0$ for simplicity. Beware that this notation of t is used solely for describing the fitting formulas and is different from the retarded time $t_{\rm ret}$ that was used in Figs. 7–11.

Taking into account the characteristic properties of gravitational waves listed above, we first introduce a fitting formula that contains 13 free parameters as follows. Using the fact that a complex function of any gravitational-wave signal $h(t)$ can be uniquely decomposed into a pair of real function $AP(t)$ and $PP(t)$ as

$$h(t) = AP(t)\exp[-iPP(t)], \tag{14}$$

we consider the following forms of fitting formulas:

$$h_{\rm fit}(t) = AP_{\rm fit}(t)\exp[-iPP_{\rm fit}(t)], \tag{15}$$

where

$$AP_{\rm fit}(t) = \left[a_1\exp\left(-\frac{t}{a_{\rm d}}\right) + a_0\right]\left(\frac{1}{1+\exp[(t-a_{\rm co})/t_{\rm cut}]}\right) \times\left[1-\exp\left(-\frac{t}{a_{\rm ci}}\right)\right], \tag{16}$$

$$PP_{\rm fit}(t) = p_0 + p_1 t + p_2 t^2 + p_3 t^3 + \exp\left(-\frac{t}{p_{\rm d}}\right)[p_{\rm c}\cos(p_{\rm f}t) + p_{\rm s}\sin(p_{\rm f}t)]. \tag{17}$$

Equation (16) shows that we model the fitting function for the amplitude part in terms of three parts:

(1) $a_1 e^{-t/a_{\rm d}} + a_0$ denotes the evolution for the amplitude which is assumed to be composed of an exponentially damping term and a constant term. a_0,

a_1, and a_d are free parameters that should be determined by a fitting procedure.

(2) $[1 + \exp\{(t - a_{co})/t_{cut}\}]^{-1}$ denotes a cutoff term that specifies a time interval of a high-amplitude stage with a_{co} being the center of the cutoff time and t_{cut} being the time scale for the shutdown. $a_{co} <$ 10 ms for the case that a black hole is formed within 10 ms after the formation of a MNS. a_{co} is determined in the fitting process, while t_{cut} is a parameter that should be manually chosen and fixed; we here choose it to be 0.1 ms for simplicity.

(3) $1 - \exp(-t/a_{ci})$ is a steeply increasing function for $t \gtrsim t_i$ with a_{ci} being the growth time scale. The reason for introducing this term is that at $t = t_i = 0$, the amplitude of gravitational waves is universally low, but after this moment, the amplitude steeply increases and the time scale depends on the total mass, mass ratio, and EOS (see waveforms in Sec. IV).

We note that in this fitting formula, we do not take into account the effect of the modulation in the amplitude: To do so, we have to significantly increase the number of fitting parameters. However these additional parameters increase the search costs, and hence, in this paper we focus on a relatively simple fitting formula.

Equation (17) shows that we model the fitting function for the frequency in terms of a secularly evolving term $p_0 + p_1 t + p_2 t^2 + p_3 t^3$ and damping oscillation term $e^{-t/p_d}[p_c \cos(p_f t) + p_s \sin(p_f t)]$. Here, eight constants p_0, p_1, p_2, p_3, p_d, p_f, p_c, and p_s are free parameters that should be determined by a fitting procedure.

Thus, in total, there are 13 parameters to be determined, and we denote them by $\vec{Q}$ in the following. We here stress that 13 parameters are the maximally necessary ones in our present fitting procedure. In the following, we ask whether it is possible to reduce the number as small as possible.

B. Determining the model parameters

1. Fitting procedure

First, we focus on the fitting formula that contains 13 parameters and describe how we determine these parameters. For the determination, it might be natural to define the following function:

$$\mathcal{M}(h_{fit}) := \frac{(h_{NR}, h_{fit})}{\sqrt{(h_{NR}, h_{NR})(h_{fit}, h_{fit})}}, \tag{18}$$

and consider maximizing the absolute value of this function. Here, $(\cdot, \cdot)$ is the inner product defined in the time domain by

$$(a, b) := \mathrm{Re}\left(\int_{t_i}^{t_f} a(t) b^*(t) dt\right), \tag{19}$$

and we note that the maximum value of $\mathcal{M}(h_{fit})$ is unity.

One problem to be pointed out is that Eq. (18) has a freedom of the scale transformation as $h_{fit} \to C h_{fit}$ with C being an arbitrary constant, and hence, the amplitude of the fitting function cannot be determined by maximizing $\mathcal{M}$. Thus, as an alternative, we define the following *cost function*:

$$C_C(h_{fit}) := -\mathcal{M}(h_{fit}) + \frac{[(h_{NR}, h_{NR}) - (h_{fit}, h_{fit})]^2}{(h_{NR}, h_{NR})^2}, \tag{20}$$

and consider minimizing this function. Here, the second term is in a sense the normalization factor by which the ambiguity in the amplitude of h_{fit} is fixed. We note that by the minimization of C_C, we can obtain h_{fit} that maximizes $\mathcal{M}$ and also the amplitude of h_{fit} that agrees approximately with that of h_{NR}.

We use a CMA-ES (covariance matrix adaption evolution search) algorithm [53–55] to solve the minimization problems. CMA-ES is a widely applicable optimization method for N-input, 1-output real-valued functions $y = f(\vec{x})$. CMA-ES belongs to a category of stochastic optimization algorithms such as, e.g., Markov chain Monte Carlo methods and genetic algorithms. The CMA-ES algorithm keeps track of a multivariate normal distribution $\mathcal{N}(\mu, \Sigma)$ from which guess parameters $\vec{x}$ are generated. The CMA-ES algorithm proceeds by updating the mean μ and the covariance matrix Σ according to the values of $f(\vec{x})$ for randomly sampled $\vec{x}$. Because of this, CMA-ES has many preferable properties: It does not require the information of $\nabla f(\vec{x})$, the values of which are computationally expensive, inaccurate or inaccessible in many cases, it is robust against noise in f and/or tiny local minima in f, its result is not affected by composing any increasing function g on the output space $g(f(\vec{x}))$, and its result is also not affected by Affine transformation in the input space $f(A\vec{x} + \vec{b})$ if the initial distribution is also modified by the inverse transformation.

Despite such properties, minimizing $C_C(h_{fit})$ is not straightforwardly achieved by CMA-ES because the function has lots of local minima in its 13-dimensional parameter space. Therefore, we resort to metaheuristics that decompose the main problem into multiple optimization subproblems, each of which is solved by the CMA-ES algorithm.

To begin with, we introduce two supplementary cost functions as

$$C_P(h_{fit}) := \int_{t_i}^{t_f} AP_{NR}^2 (PP_{NR} - PP_{fit})^2 dt, \tag{21}$$

$$C_A(h_{fit}) := \int_{t_i}^{t_f} (AP_{NR} - AP_{fit})^2 dt, \tag{22}$$

where AP_{NR} and PP_{NR} are amplitude and phase parts of h_{NR}, respectively, which are obtained by the decomposition defined in Eq. (14). Then, instead of performing the minimization procedure in the 13-parameter space altogether, we

TABLE IV. A procedure of determining 13 parameters is illustrated. The procedure in this example is composed of 9 steps. In the first–fifth steps, we update (p_0, p_1), (p_0, p_1, p_2), (p_0, p_1, p_2, p_3), (p_d, p_f, p_c, p_s), and all eight parameters of the phase part p_i using the cost function C_P, respectively, and in the sixth–eighth steps, five parameters in the amplitude part a_i are updated using the cost function C_A. At the ninth step, all the parameters are updated at the same time using the cost function C_C. At each step, the values of parameters determined in the previous steps are used as the initial-guess values. The leftmost letter (P or A or C) indicates the type of cost function C_P or C_A or C_C used in the corresponding step. See also the text for a more detailed description.

$N_p = 13$		p_d	p_f	p_c	p_s	p_3	p_2	p_1	p_0	a_{ci}	a_{co}	a_0	a_d	a_1
1.	(P)							○	○					
2.	(P)						○	○	○					
3.	(P)					○	○	○	○					
4.	(P)	○	○	○	○									
5.	(P)	○	○	○	○	○	○	○	○					
6.	(A)											○	○	○
7.	(A)									○		○	○	○
8.	(A)										○	○	○	○
9.	(C)	○	○	○	○	○	○	○	○	○	○	○	○	○

determine a subset of 13 parameters by a minimization procedure in terms of C_P and C_A step by step.

Table IV shows an example of the parameter-search procedure. In this example, 13 parameters of a waveform are eventually updated after the following nine steps (the step indices correspond to those in Table IV):

(0) In the beginning, we give initial-guess values (see Sec. V B 2) for all 13 parameters.
(1) In the first step, we update parameters (p_0, p_1) by minimizing the cost function C_P.
(2) Using the new set of (p_0, p_1) as a part of the updated initial-guess parameters, we update (p_0, p_1, p_2).
(3) Similarly, parameters (p_0, p_1, p_2, p_3) are updated in the third step.
(4) The parameters of the damping oscillation term in phase (p_d, p_f, p_c, p_s) are updated using the cost function C_P and fixing (p_0, p_1, p_2, p_3) to be the values obtained in the previous step.
(5) All of the parameters in phase $(p_d - p_s$ and $p_0 - p_3)$ are updated starting from the values obtained in the first–fourth steps as the initial guess and employing C_P as the cost function.
(6) We update the exponentially damping term in amplitude (a_0, a_1, a_d) employing C_A as the cost function. Here, we fix the values of all the eight parameters in phase $(p_d - p_3)$ to be those determined in the fifth step.
(7) We update the parameters for the steeply increasing term (a_{ci}), with three other parameters in amplitude (a_0, a_1, a_d) also subject to change.
(8) We update the parameters for the cutoff term (a_{co}) in a similar manner.
(9) Finally, we minimize the cost function C_C using all of the parameters obtained up to the eighth step as the initial guess.

This procedure should be iterated until the sufficient convergence is achieved.

The circles in each row of Table IV denote the parameters that are updated at each step. For the fitting procedure at each step, we use the CMA-ES algorithm. Note that in

TABLE V. The standard values of parameters $\vec{Q}_{std}$, their deviations σ_{std}, and their constraints.

Parameter $(Q_{std} \pm \sigma_{std})$		Dimension	Constraints
$a_1 = 0.113793577854$	± 0.2	1	$a_1 > 0$
$a_d = 3.61810442878 \times 10^{-3}$	± 0.01	s	
$a_0 = 6.67194850219 \times 10^{-3}$	$\pm 1 \times 10^{-3}$	1	$a_0 > 0$
$a_{co} = 0.012$	± 0.01	s	$3 \times 10^{-4} < a_{co} < 1.2 \times 10^{-2}$
$a_{ci} = 2.28934356228 \times 10^{-4}$	$\pm 5 \times 10^{-4}$	s	
$p_0 = 4.12034039189$	± 37	1	
$p_1 = 1.56534759719 \times 10^4$	$\pm 4 \times 10^3$	s^{-1}	
$p_2 = 0$	$\pm 3 \times 10^5$	s^{-2}	
$p_3 = 0$	$\pm 1 \times 10^7$	s^{-3}	
$p_s = 0.494703128127$	± 1	1	
$p_c = -0.116384976953$	± 1	1	
$p_f = 6.607469741287686 \times 10^3$	$\pm 1 \times 10^3$	s^{-1}	$p_f > 0$
$p_d = 1.69866461255 \times 10^{-3}$	$\pm 2 \times 10^3$	s	

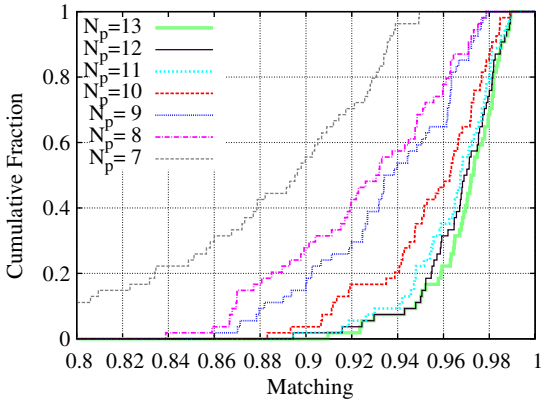

FIG. 14 (color online). Cumulative distribution of the maximum value of $\mathcal{M}$ for the parameter fitting with the number of parameters $N_{\rm p} = 7$–13. The horizontal axis denotes the maximum value of matching $\mathcal{M}$ and the vertical axis shows the cumulative fraction of the models whose maximum fitting value is less than $\mathcal{M}$.

the above procedure, we employ the cost function $C_{\rm P}$ when all the target parameters belong to the phase part (PP), while we employ $C_{\rm A}$ when all the target parameters belong to the amplitude part (AP). We employ $C_{\rm C}$ only when the parameters in the search include parameters of both (AP) and (PP) parts.

2. Standard set of the 13 parameters

The CMA-ES algorithm requires the values and deviations of the initial guess for all the input parameters. As the search procedure proceeds, we can obtain accumulated sets of 13 parameters determined in the different cycles of search procedures and for additional models. By taking median over them, we may construct a standard set of the 13 parameters, which can be used as the initial guess in the search procedure that follows. Table V denotes the standard set of the parameters $\vec{Q}_{\rm std}$ and their deviations $\sigma_{\rm std}$ which were obtained from the results of the search for all the numerical waveforms employed in this paper. Here, we artificially set p_2 and p_3 to be zero because we want to always test the quality of the fitting functions that are linear in time for the phase part. Note that this standard set will be improved as the search procedure proceeds and as more waveforms are involved. We use the determined 13 parameters for a set of the waveforms as an initial guess in the next generation of fitting.

C. Fitting results

Figure 14 shows the cumulative distribution for the maximum value of $\mathcal{M}$. Here, see the plot for $N_{\rm p} = 13$ that denotes the cumulative distribution for the case of the 13-parameter fitting (see also the column of $\mathcal{M}_{N_{\rm p}=13}$ in Table III which lists the maximum values of $\mathcal{M}$ for all the numerical waveforms). This plot shows that for $\sim$90% of the waveforms, the maximum value of $\mathcal{M}$ is larger than 0.95. Also for all the waveforms, the maximum value of $\mathcal{M}$ is larger than 0.90.

Figure 15 compares numerical waveforms with their fitting results for four models, for all of which the value of $\mathcal{M}$ is larger than 0.98. For these models, the amplitude of gravitational waves emitted by a MNS decreases monotonically with time and the corresponding frequency is approximately constant only with small modulation. For this type of the waveforms, the fitting can be well achieved in our fitting formula.

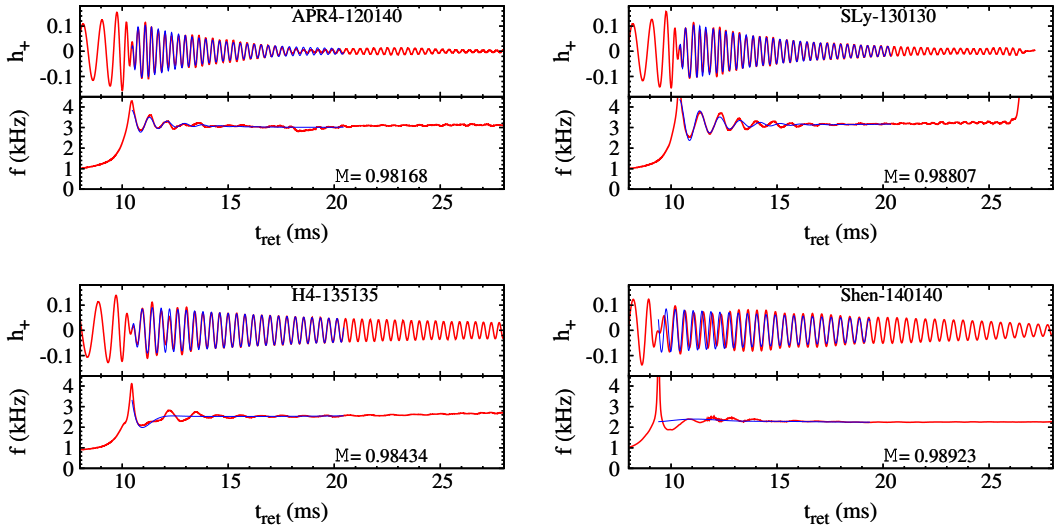

FIG. 15 (color online). Comparison of numerical waveforms with their fitting results for APR4-120140, SLy-130130, H4-135135 with $\Gamma_{\rm th} = 1.8$ and Shen-140140. Gravitational waves ($h_+ D/m$) and the frequency of gravitational waves f (kHz) as functions of retarded time are plotted. The red (thick) curves are numerical waveforms, as in Fig. 7, while the blue (thin) segment curves are the corresponding fitting functions with the best-fit parameters. The numerical value written in the lower right corner of each panel is the value of $\mathcal{M}$.

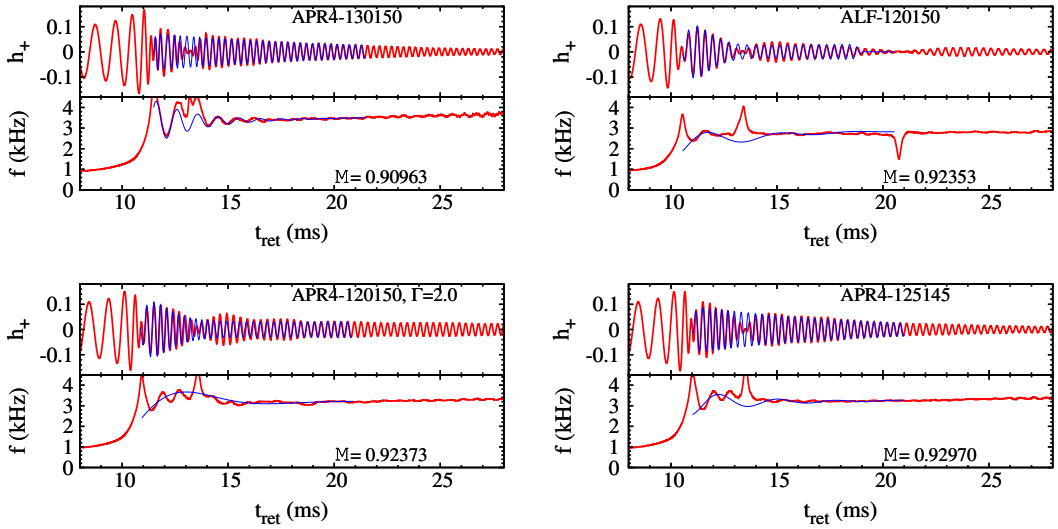

FIG. 16 (color online). The same as Fig. 15 but for APR4-130150, ALF2-120150, APR4-120150 (with $\Gamma_{\rm th} = 2.0$), and APR4-125145. This figure shows that our fitting formula (15) is relatively poor at fitting the modulating feature in the amplitude.

By contrast, the fitting is not as well achieved for the case that the amplitude significantly modulates with time in the early phase of the MNS evolution. Figure 16 shows the sample for such cases. For all the models picked up in this figure, the amplitude increases with time from $t = t_i$ and reaches a high value. Then, the amplitude once damps at $t - t_i = 2$–5 ms, and subsequently, quasiperiodic gravitational waves with slowly decreasing amplitude are emitted. This type of gravitational waveform is often found for the case of asymmetric binaries with APR4 and ALF2. Nevertheless, the value of $\mathcal{M}$ is still larger than 0.9.

We notice that the fitting formula, which is constructed with the data for 10 ms duration, could reproduce longer data as well (e.g., 20 ms data). Indeed, the value of $\mathcal{M}$ for 20 ms duration data with the fitting formula is only 1% smaller than the value of $\mathcal{M}$ listed in Table III for the compact neutron star models, APR4, SLy, and ALF2. For the less compact neutron star models, the value of $\mathcal{M}$ is still 1%–10% smaller than the value listed in Table III. For the softer EOSs, the duration of high-amplitude gravitational waves is relatively short as $\lesssim 10$ ms. Thus, the longer data do not contribute much to the matching. This is the reason that the value of $\mathcal{M}$ depends weakly on the duration of the data. For the stiffer EOSs, in particular, for H4, the duration of high-amplitude gravitational waves is longer as $\gtrsim 10$ ms. For such gravitational waves, the matching parameters have to be reconstructed for the longer-duration data.

Before closing this subsection, we comment on the convergence of the value of $\mathcal{M}$. For the case that the gravitational waveform has the modulation of the amplitude, the value of $\mathcal{M}$ is lower for the higher-resolution simulations, because the modulation of the amplitude is more distinctive for the higher-resolution simulations (see details in Appendix A). Therefore the value of $\mathcal{M}$ is likely to be overestimated for the waveforms which have the large modulation.

D. Reduction of the number of the free parameters

We now explore possible fitting formulas in which the number of free parameters is smaller than 13; some of the 13 parameters are fixed to particular values. A question to ask in the reduction process is whether the search output in the fitting formula composed of 13 parameters is insensitive to some of the parameters. If this is the case, we could effectively reduce the search space by fixing such insensitive parameters to standard values. In fact this is the case: We can construct fitting formulas that preserve nearly the same quality even when we reduce the number of free parameters to ~ 11, as we can see in Figs. 14 and 17.

To access the quality of the reduced fitting formula, in this paper, we introduce a quality function $q(\vec{\rm Q}')$ for a subset of parameters $\vec{\rm Q}' \subset \vec{\rm Q}$. $q(\vec{\rm Q}')$ is defined as the worst value among the maximum values of $\mathcal{M}$ when the fitting is performed only for the subset of parameters $\vec{\rm Q}'$:

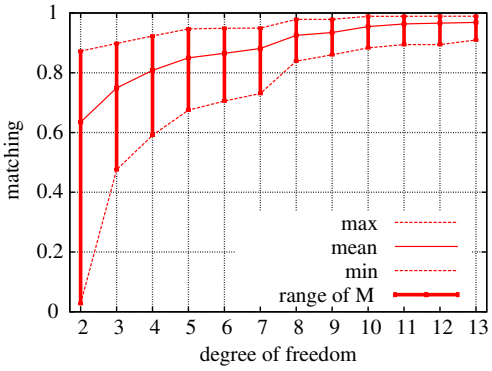

FIG. 17 (color online). Summary of the performance of the best-fitting procedures as a function of the number of parameters. The maximum, minimum, and mean values of $\mathcal{M}(h)$ for the best-fitting procedures are shown. The procedure with the largest quality $q = \mathcal{M}(\arg_h \min(h))$ is defined as the best one.

TABLE VI. The sets of free parameters in the chosen fitting formulas with $N_{\rm p} = 2$–13. The value of $\mathcal{M}$ is not very sensitive to $a_{\rm co}$ and p_s if the standard values listed in Table V are assigned.

	Phase part								Amplitude part					Quality
$N_{\rm p} = 2$							p_1	p_0						0.0274881661358768
$N_{\rm p} = 3$							p_1	p_0				$a_{\rm d}$		0.4753105281276069
$N_{\rm p} = 4$			$p_{\rm c}$				p_1	p_0				$a_{\rm d}$		0.5908178259595284
$N_{\rm p} = 5$			$p_{\rm c}$				p_1	p_0	$a_{\rm ci}$			$a_{\rm d}$		0.6750096266165332
$N_{\rm p} = 6$			$p_{\rm c}$				p_1	p_0	$a_{\rm ci}$			$a_{\rm d}$	a_1	0.7053957819403283
$N_{\rm p} = 7$			$p_{\rm c}$			p_2	p_1	p_0	$a_{\rm ci}$			$a_{\rm d}$	a_1	0.7305212430130907
$N_{\rm p} = 8$	$p_{\rm d}$		$p_{\rm c}$			p_2	p_1	p_0	$a_{\rm ci}$			$a_{\rm d}$	a_1	0.8388076222568087
$N_{\rm p} = 9$	$p_{\rm d}$		$p_{\rm c}$			p_2	p_1	p_0	$a_{\rm ci}$		a_0	$a_{\rm d}$	a_1	0.8600728396291507
$N_{\rm p} = 10$	$p_{\rm d}$	$p_{\rm f}$	$p_{\rm c}$			p_2	p_1	p_0	$a_{\rm ci}$		a_0	$a_{\rm d}$	a_1	0.8831675719064657
$N_{\rm p} = 11$	$p_{\rm d}$	$p_{\rm f}$	$p_{\rm c}$		p_3	p_2	p_1	p_0	$a_{\rm ci}$		a_0	$a_{\rm d}$	a_1	0.8943981384792208
$N_{\rm p} = 12$	$p_{\rm d}$	$p_{\rm f}$	$p_{\rm c}$	p_s	p_3	p_2	p_1	p_0	$a_{\rm ci}$		a_0	$a_{\rm d}$	a_1	0.8943981384792208
$N_{\rm p} = 13$	$p_{\rm d}$	$p_{\rm f}$	$p_{\rm c}$	p_s	p_3	p_2	p_1	p_0	$a_{\rm ci}$	$a_{\rm co}$	a_0	$a_{\rm d}$	a_1	0.9096283876761225

$$q(\vec{\rm Q}') := \min_{\rm NR\ models}[\mathcal{M}(h_{\rm fit})]. \tag{23}$$

Then, we consider that the quality of a fitting formula is better if the values of $q(\vec{\rm Q}')$ is larger.

We employ a simple heuristics to reduce the number of free parameters starting from 13 free parameters obtained in the best-fitting formula as follows:

(1) We can construct a *reduced* formula with 12 free parameters, by fixing one of the parameters to the standard value (listed in Table V).
(2) We measure the quality of all the reduced formulas by performing fitting procedure described in Sec. V B for each of them.
(3) We choose the reduced formula with the highest quality and consider it as the best formula in the 12-parameter search.

We further repeat this to construct a reduced formula with 11 free parameters, starting from the best formula in the 12-parameter search. In general, we can define a reduced formula with $(N_{\rm p} - 1)$ free parameters from a $N_{\rm p}$-parameter formula, by choosing the free parameter that has the least effect on the quality and by fixing it. In this manner, we constructed 11 reduced formulas with $N_{\rm p} = 2$–12.

In the above heuristics, we search only for small subspaces of all the possible parameter reduction spaces. To confirm that our choice for the parameter reduction would be the best one, we also tested other heuristics for reducing the number of parameters. We also tried several different formulas for the same choice of $\vec{\rm Q}'$.

Also, it was sometimes found that for certain waveforms, an increase in $N_{\rm p}$ could result in the decrease of $\mathcal{M}$. This may seem counterintuitive, but in reality such a miss fitting is inevitable. This is because $\mathcal{M}$ is assured to be the increasing function of $N_{\rm p}$ only if the global optima are always obtained. However, in practice, a fake solution, which falls into a local minimum, is often obtained, and hence, it is not easy to achieve the global optimization. When we found such decrease in $\mathcal{M}$, we performed the fitting for a larger value of $N_{\rm p}$ again, using the results of fitting obtained from a lesser value of $N_{\rm p}$ as the initial guess.

An update in the standard set of parameters may also result in the decrease of the quality for some of the reduced formulas. In such cases, we can also reuse the results from the past overwriting the fitting results for all the waveforms consistently. The number of the degrees of freedom is still $N_{\rm p}$ after such operations. We can understand this visually in the following way: What we call a reduced formula corresponds to an $N_{\rm p}$-dimensional plane embedded in the 13-dimensional parameter space, and locally adopting a different "standard set of parameters" corresponds to a parallel displacement of the $N_{\rm p}$-dimensional plane in the 13-dimensional space.

E. Results of the parameter reduction

Table III lists the maximum values of $\mathcal{M}$ for the cases of $N_{\rm p} = 10$–13 parameters (see the columns $\mathcal{M}_{N_{\rm p}=10}$ to $\mathcal{M}_{N_{\rm p}=13}$). This table obviously shows that the maximum values of $\mathcal{M}$ are approximately identical for $N_{\rm p} = 12$ and $N_{\rm p} = 13$ (except for APR4-130150 and ALF-140140). Therefore, the cumulative distributions for these two cases are approximately identical as that found in Fig. 14 (see the plots for $N_{\rm p} = 12$ and 13). This implies that the search procedure may well be performed in the fitting formula with 12 free parameters fixing $a_{\rm co}$, which might be a redundant parameter.

We further perform the reduction, and construct reduced fitting formulas with 2–11 free parameters ($N_{\rm p} = 2$–11). We list the sets of the parameters for $N_{\rm p} = 2$–13 in Table VI. Figure 14 shows the cumulative distribution of $\mathcal{M}$ for the formulas with $N_{\rm p} = 7$–13. Figure 17 shows the qualities of reduced formulas as a function of the number of parameters. This figure indicates that the reduced

formula with $N_{\rm p} = 11$–13 have approximately the same quality, giving $\mathcal{M} > 0.9$ for more than 98% of the waveforms. The reduced formulas with $N_{\rm p} = 8$–10 have a gradually decreasing quality, giving $\mathcal{M} > 0.9$ for $\gtrsim 80\%$ of the waveforms. Then, there is a substantial quality gap between $N_{\rm p} = 7$ and $N_{\rm p} = 8$. This occurs when $p_{\rm d}$ is fixed to its standard value.

The last two columns of Table III also list the values of $\mathcal{M}_{M_{\rm p}=11}$ and $\mathcal{M}_{M_{\rm p}=10}$. Comparing these data with $\mathcal{M}_{M_{\rm p}=13}$ also shows that the reduced formula with $N_{\rm p} = 11$ has the quality that is approximately the same as that for $N_{\rm p} = 13$. This implies that we may reduce the number of the parameters to 11 by fixing the values of the other parameters to be the standard values. We may further reduce the number of free parameters to 10 if we can allow the matching with $\mathcal{M} < 0.9$ for $\sim 5\%$ of the waveforms.

VI. SUMMARY

The latest discoveries of high-mass neutron stars with mass $1.97 \pm 0.04 M_\odot$ [14] and $2.01 \pm 0.04 M_\odot$ [15] constrain that the maximum mass of (cold) spherical neutron stars for a given hypothetical EOS has to be larger than $\sim 2 M_\odot$, and suggests that the EOS of neutron stars has to be quite stiff. We performed a number of numerical-relativity simulations employing stiff EOSs with a variety of the plausible total mass and mass ratio of binary neutron stars. We found that for the canonical total mass of binary neutron stars $m \approx 2.7 M_\odot$, not a black hole but a MNS is the canonical remnant, and that for many cases, it is a HMNS. The MNSs are rapidly rotating and nonaxisymmetric, and thus, they are often strong emitters of quasiperiodic gravitational waves and efficiently exert the torque to the envelope surrounding them. We explored the evolution processes of the remnant MNSs and found that their lifetime is much longer than the dynamical time scale of the system $\gg 1$ ms for most models. Their lifetime also depends strongly on the EOSs and their total mass, although they should always collapse to a black hole eventually if they are hypermassive.

We classified the final fate of the MNSs by specifying what determines their evolution time scale. There are at least four ingredients that affect the evolution of the MNSs: gravitational-wave emission, angular-momentum transport via a hydrodynamical process associated with the nonaxisymmetric structure of the MNSs, angular-momentum transport process via magnetohydrodynamical processes such as magnetic winding and MRI, and neutrino cooling. If the gravitational-wave emission and hydrodynamical angular-momentum transport determine the evolution of a HMNS, its nonaxisymmetry plays a crucial role and hence its lifetime will be short, $\lesssim 100$ ms. If a HMNS is alive for a longer time, magnetorotational processes are likely to play an important role [40]: After a substantial amount of angular momentum is transported outward, the HMNS will collapse to a black hole. If the system is not massive enough, the angular-momentum transport alone is not likely to trigger the collapse to a black hole. For such a system, neutrino cooling will play an important role (e.g., [10,11]). If the system is hypermassive but the thermal pressure significantly contributes to sustaining the self-gravity of the HMNS, the collapse will occur in the neutrino cooling time scale of seconds. If the system is not hypermassive but supramassive, the SMNS will be alive for a time longer than the cooling time scale. Their lifetime will be determined by the dissipation time scale of angular momentum such as magnetic dipole radiation.

In the later part of this paper, we studied in detail the properties of quasiperiodic gravitational waves emitted by MNSs. We found that the gravitational waveforms well reflect the evolution process of the MNSs. Basically, the waveforms have the following universal features: they are quasiperiodic with an approximately constant frequency ~ 2–3.5 kHz, although the frequency changes with time in particular in the early stage of the MNSs, the time-variation part of the frequency is composed of an early high-amplitude oscillation and a subsequent secular variation, and the amplitude decreases (approximately) monotonically with time scale $\gtrsim 10$ ms which is much longer than the oscillation period and dynamical time scale of the MNSs. Taking into account these universal features of the gravitational waveforms, we constructed a fitting formula that is used for modeling gravitational waves of a variety of MNSs irrespective of EOSs and the values of binary mass. It is found that the waveforms are well fitted by 13 parameter models with the value of the matching factors >0.90 for all the waveforms and >0.95 for $\sim 90\%$ of the waveforms. Even with 11 parameter models, the value of the matching factors is larger than 0.90 for 98% of the waveforms and $\gtrsim 0.95$ for $\sim 75\%$ of the waveforms.

We also found a correlation between the characteristic frequency of gravitational waves emitted by MNSs and a neutron star radius, as found in [23]. However, it was also clarified that the frequency has a systematic dispersion because it changes with time during the evolution of the MNSs. Because of this systematic component, the correlation relation is not as sharp as that pointed out in [23], and thus, we conclude that even if the characteristic frequency is determined accurately, the systematic error for the estimation of the neutron star radius of ~ 1 km will be inevitable. Nevertheless, the neutron star radius is constrained strongly, and therefore, measuring the characteristic frequency is an important subject in the future gravitational-wave observation.

ACKNOWLEDGMENTS

We thank M. Ando, T. Nakamura, and H. Tagoshi for fruitful discussions on the data analysis of gravitational

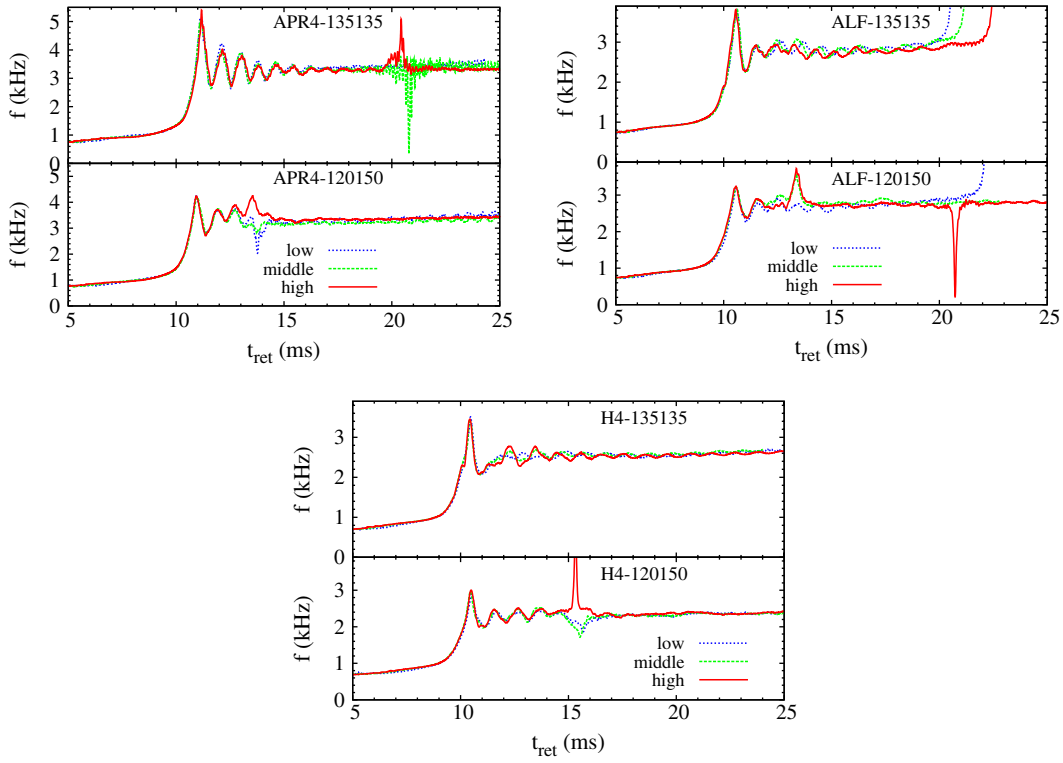

FIG. 18 (color online). The resolution study for the evolution of the frequency of gravitational waves emitted by MNSs for APR4, ALF2, and H4 EOSs with $m_1 = m_2 = 1.35M_\odot$ and $(m_1, m_2) = (1.2M_\odot, 1.5M_\odot)$. For each model, three grid resolutions are chosen; see Sec. IIB and Table V of [12]. For aligning the curve at the onset of the merger, the time is shifted for the data of low and middle resolutions. Spikes found for the plots of APR4-135135, APR4-120150, ALF-120150, and H4-120150 are not physical; these are generated when the gravitational-wave amplitude is too low to determine the frequency accurately.

waves. This work was supported by Grants-in-Aid for Scientific Research (No. 21340051, No. 21684014, No. 24244028, No. 24740163), by Grants-in-Aid for Scientific Research on an Innovative Area (No. 20105004, No. 24103506), and the HPCI Strategic Program of Japanese MEXT. This work was partly supported by the "Joint Usage/Research Center for Interdisciplinary Large-Scale Information Infrastructures" in Japan. The work of K. K. is supported by a JSPS Postdoctoral Fellowship for Research Abroad. The work of K. H. was supported by the Grant-in-Aid of JSPS.

APPENDIX: CONVERGENCE

When we model a gravitational waveform in terms of our fitting formula, the most important quantity is its frequency. We here show the convergence property for the numerical results of the frequency of gravitational waveforms emitted by MNSs. Figure 18 plots the frequency as a function of $t_{\rm ret}$ for APR4, ALF2, and H4 EOSs with $m_1 = m_2 = 1.35M_\odot$ and $(m_1, m_2) = (1.2M_\odot, 1.5M_\odot)$ for typical examples. For each model, three grid resolutions are chosen (see Sec. II B and Table V of [12]). We also provide the average frequency

TABLE VII. The resolution study for the characteristic frequency $f_{\rm ave,10ms}$ and the maximum values of $\mathcal{M}$ for APR4, ALF2, and H4 EOSs with $m_1 = m_2 = 1.35M_\odot$ and $(m_1, m_2) = (1.2M_\odot, 1.5M_\odot)$. Here the number of parameters is set to be $N_{\rm p} = 13$.

Model	$f^{\rm low}_{\rm ave,10\,ms}$ (kHz)	$f^{\rm middle}_{\rm ave,10\,ms}$ (kHz)	$f^{\rm high}_{\rm ave,10\,ms}$ (kHz)	$\mathcal{M}_{\rm low}$	$\mathcal{M}_{\rm middle}$	$\mathcal{M}_{\rm high}$
APR4-120150	3.31 ± 0.23	3.28 ± 0.23	3.41 ± 0.24	0.964	0.972	0.959
APR4-135135	3.40 ± 0.36	3.34 ± 0.36	3.28 ± 0.37	0.970	0.981	0.970
ALF2-120150	2.68 ± 0.13	2.78 ± 0.15	2.71 ± 0.16	0.991	0.975	0.924
ALF2-135135	2.82 ± 0.21	2.82 ± 0.19	2.76 ± 0.15	0.988	0.990	0.989
H4-120150	2.27 ± 0.12	2.28 ± 0.14	2.31 ± 0.15	0.986	0.984	0.964
H4-135135	2.51 ± 0.14	2.52 ± 0.14	2.48 ± 0.16	0.982	0.990	0.984

and the maximum value of $\mathcal{M}$ for those models in Table VII.

As we described in [12], the peak frequency of the Fourier spectrum and the averaged value of the frequency converge within $\sim$0.1 kHz error and the error is smaller than the systematic dispersion σ_f. The convergence for the stiffer EOS such as H4 is better than that for the softer EOS such as APR4. The possible reason for this is that neutron stars for the stiffer EOSs are less compact and shock heating effects are weaker that those for the softer EOS. (Note that in the presence of shocks the convergence is achieved only at the first order.) Similarly, the values of the frequency are found to converge to this level at each stage of MNSs except for the case that a black holes is formed; for this case, the frequency varies steeply with time and the convergence at a given moment is relatively poor.

As already noted in the caption of Fig. 7, spikes found for the plots of APR4-135135, APR4-120150, ALF-120150, and H4-120150 are not physical; these are generated when the gravitational-wave amplitude is quite low and hence the frequency cannot be determined accurately. Such spikes do not play a serious role for determining the Fourier spectrum, averaged frequency, and σ_f because the gravitational-wave amplitude is small at a moment that the spikes are generated. For instance, the difference in the averaged frequency between H4-120150 (low) and H4-120150 (high), which includes a spike, is only 2%.

For ALF, a black hole is formed in a relatively short time scale; see, e.g., the plot of ALF-135135. This plot illustrates that for the lower resolution, the lifetime of the HMNS is shorter. This is also the case for ALF-120150. As pointed out in the last paragraph of Sec. III B, this is an often-found property of our numerical simulations.

The value of $\mathcal{M}$ depends on the grid resolution of the simulation (see Table VII). For equal-mass models, the value of $\mathcal{M}$ varies only about 0.01 depending on the grid resolution. For unequal-mass models, the dependence of the value of $\mathcal{M}$ on the grid resolution is stronger than that of the equal-mass models. Moreover, the value of $\mathcal{M}$ is the lowest for the waveform of the highest-resolution simulations. The reason is as explained in Sec. V C: For unequal-mass models, the gravitational-wave amplitude modulates significantly at 2–5 ms after the merger (see, e.g., Fig. 8). The shape of the modulation is more distinctive for the waveform of the higher resolution simulation. It is difficult for the fitting function, Eqs. (15)–(17), to deal with such modulation in the gravitational-wave amplitude. Therefore the value of $\mathcal{M}$ is low for the highest-resolution simulations. To increase the value of $\mathcal{M}$ for these models we would have to increase the number of the parameters of our fitting formula.

[1] J. Abadie *et al.*, Nucl. Instrum. Methods Phys. Res., Sect. A **624**, 223 (2010); T. Accadia *et al.*, Classical Quantum Gravity **28**, 025005 (2011); K. Kuroda *et al.*, Classical Quantum Gravity **27**, 084004 (2010).

[2] V. Kalogera, K. Belczynski, C. Kim, R. Oshaughnessy, and B. Willems, Phys. Rep. **442**, 75 (2007).

[3] J. Abadie *et al.*, Classical Quantum Gravity **27**, 173001 (2010).

[4] E. E. Flanagan, and T. Hinderer, Phys. Rev. D **77**, 021502 (R) (2008); T. Hinderer, B. D. Lackey, R. N. Lang, and J. S. Read, Phys. Rev. D **81**, 123016 (2010); T. Damour, A. Nagar, and L. Villain, Phys. Rev. D **85**, 123007 (2012); J. S. Read, L. Baiotti, J. D. E. Creighton, J. L. Friedman, B. Giacomazzo, K. Kyutoku, C. Markakis, L. Rezzolla, M. Shibata, and K. Taniguchi, arXiv:1306.4065 [Phys. Rev. D (to be published)].

[5] T. W. Baumgarte, S. L. Shapiro, and M. Shibata, Astrophys. J. Lett. **528**, L29 (2000).

[6] G. B. Cook, S. L. Shapiro, and S. A Teukolsky, Astrophys. J. **398**, 203 (1992).

[7] G. B. Cook, S. L. Shapiro, and S. A Teukolsky, Astrophys. J. **424**, 823 (1994).

[8] M. Shibata, K. Taniguchi, and K. Uryū, Phys. Rev. D **71**, 084021 (2005); M. Shibata and K. Taniguchi, Phys. Rev. D **73**, 064027 (2006); K. Kiuchi, Y. I. Sekiguchi, M. Shibata, and K. Taniguchi, Phys. Rev. D **80**, 064037 (2009).

[9] K. Hotokezaka, K. Kyutoku, H. Okawa, M. Shibata, and K. Kiuchi, Phys. Rev. D **83**, 124008 (2011).

[10] Y. Sekiguchi, K. Kiuchi, K. Kyutoku, and M. Shibata, Phys. Rev. Lett. **107**, 051102 (2011); Prog. Theor. Exp. Phys. **01**, A304 (2012).

[11] Y. Sekiguchi, K. Kiuchi, K. Kyutoku, and M. Shibata, Phys. Rev. Lett. **107**, 211101 (2011).

[12] K. Hotokezaka, K. Kiuchi, K. Kyutoku, H. Okawa, Y. Sekiguchi, M. Shibata, and K. Taniguchi, Phys. Rev. D **87**, 024001 (2013).

[13] J. M. Lattimer and M. Prakash, Science **304**, 536 (2004); Phys. Rep. **442**, 109 (2007).

[14] P. Demorest, T. Pennucci, S. Ransom, M. Roberts, and J. Hessels, Nature (London) **467**, 1081 (2010).

[15] J. Antoniadis *et al.*, Science **340**, 1233232 (2013).

[16] M. Shibata and K. Uryū, Phys. Rev. D **61**, 064001 (2000).

[17] M. D. Duez, Classical Quantum Gravity **27**, 114002 (2010).

[18] J. A. Faber and F. A. Radio, Living Rev. Relativity **15**, 8 (2012).

[19] L. Rezzolla, L. Baiotti, B. Giacomazzo, D. Link, and J. A. Font, Classical Quantum Gravity **27**, 114105 (2010); L. Rezzolla, B. Giacomazzo, L. Baiotti,

J. Granot, C. Kouveliotou, and M. A. Aloy, Astrophys. J. Lett. **732**, L6 (2011).
[20] M. Thierfelder, S. Bernuzzi, and B. Brügmann, Phys. Rev. D **84**, 044012 (2011); S. Bernuzzi, M. Thierfelder, and B. Brügmann, Phys. Rev. D **85**, 104030 (2012).
[21] V. Paschalidis, Z. B. Etienne, and S. L. Shapiro, Phys. Rev. D **86**, 064032 (2012).
[22] K. Kiuchi, K. Kyutoku, K. Hotokezaka, Y. Sekiguchi, and M. Shibata (unpublished).
[23] A. Bauswein and H.-Th. Janka, Phys. Rev. Lett. **108**, 011101 (2012); A. Bauswein, H.-Th. Janka, K. Hebeler, and A Schwenk, Phys. Rev. D **86**, 063001 (2012).
[24] We assume general relativity is the correct theory of gravity on the scale of neutron stars.
[25] J. S. Read, B. D. Lackey, B. J. Owen, and J. L. Friedman, Phys. Rev. D **79**, 124032 (2009).
[26] H. Shen, H. Toki, K. Oyamatsu, and K. Sumiyoshi, Nucl. Phys. **A637**, 435 (1998); Prog. Theor. Phys. **100**, 1013 (1998).
[27] H. Shen, F. Yang, and H. Toki, Prog. Theor. Phys. **115**, 325 (2006).
[28] A. Akmal, V. R. Pandharipande, and D. G. Ravenhall, Phys. Rev. C **58**, 1804 (1998).
[29] F. Douchin and P. Haensel, Astron. Astrophys. **380**, 151 (2001).
[30] M. Alford, M. Brady, M. Paris, and S. Reddy, Astrophys. J. **629**, 969 (2005).
[31] N. K. Glendenning and S. A. Moszkowski, Phys. Rev. Lett. **67**, 2414 (1991); B. D. Lackey, M. Nayyar, and B. J. Owen, Phys. Rev. D **73**, 024021 (2006).
[32] H. Müller and B. D. Serot, Nucl. Phys. **A606**, 508 (1996).
[33] I. H. Stairs, Science **304**, 547 (2004); D. R. Lorimer, Living Rev. Relativity **11**, 8 (2008); J. M. Lattimer and M. Prakash, arXiv:1012.3208.
[34] J. M. Lattimer and M. Prakash, Astrophys. J. **550**, 426 (2001).
[35] A. Bauswein, H.-Th. Janka, and R. Oechslin, Phys. Rev. D **82**, 084043 (2010).
[36] T. Yamamoto, M. Shibata, and K. Taniguchi, Phys. Rev. D **78**, 064054 (2008).
[37] K. Taniguchi and M. Shibata, Astrophys. J. Suppl. Ser. **188**, 187 (2010).
[38] http://www.lorene.obspm.fr/.
[39] M. D. Duez, Y.-T. Liu, S. L. Shapiro, and B. C. Stephens, Phys. Rev. D **69**, 104030 (2004).
[40] M. D. Duez, Y.-T. Liu, S. L. Shapiro, M. Shibata, and B. C. Stephens, Phys. Rev. Lett. **96**, 031101 (2006); M. Shibata, M. D. Duez, Y.-T. Liu, S. L. Shapiro, and B. C. Stephens, Phys. Rev. Lett. **96**, 031102 (2006).
[41] D. M. Siegel, R. Ciolfi, A. I. Harte, and L. Rezzolla, Phys. Rev. D **87**, 121302(R) (2013).
[42] S. A. Balbus and J. F. Hawley, Astrophys. J. **376**, 214 (1991); Rev. Mod. Phys. **70**, 1 (1998).
[43] See, e.g., S. L. Shapiro and S. A. Teukolsky, *Black Holes, White Dwarfs, and Neutron Stars* (Wiley Interscience, New York, 1983).
[44] J. D. Kaplan, C. D. Ott, E. P. O'Connor, K. Kiuchi, L. Roberts, and M. Duez, arXiv:1306.4034.
[45] M. Shibata, Phys. Rev. Lett. **94**, 201101 (2005).
[46] For SLy, this dependence of the lifetime on the mass ratio is not found. The reason is that for SLy (and APR4), a large fraction of mass is ejected from the system even for the equal-mass binary. For SLy-135135, $\sim 0.02 M_\odot$ is ejected while for SLy-120150, $\sim 0.01 M_\odot$ is ejected.
[47] R. Narayan, B. Paczynski, and T. Piran, Astrophys. J. Lett. **395**, L83 (1992); T. Piran, Rev. Mod. Phys. **76**, 1143 (2005); E. Nakar, Phys. Rep. **442**, 166 (2007).
[48] I. Bartos, P. Brady, and S. Marka, Classical Quantum Gravity **30**, 123001 (2013).
[49] K. Kyutoku, H. Okawa, M. Shibata, and K. Taniguchi, Phys. Rev. D **84**, 064018 (2011).
[50] It should be noted that irrespective of the mass ratio, the chirp mass defined by $(m_1 m_2)^{3/5} m^{-1/5}$ is approximately equal to the value for the equal-mass system $2^{-6/5} m$ within 1% error for $0.8 \leq q \leq 1$. Thus, we may approximately consider that the plots of Fig. 13 are the plots for a given value of the chirp mass. In the data analysis of the chirp signal of gravitational waves, the chirp mass will be determined accurately but the mass ratio may not be [51]. For this reason, we generated Fig. 13 for a given value of m irrespective of the mass ratio.
[51] C. Cutler and E. E. Flanagan, Phys. Rev. D **49**, 2658 (1994).
[52] Here we choose only the data of which the maximum mass of given EOS is larger than $1.97 M_\odot$ (see the details in Table II of [23]).
[53] N. Hansen, *The CMA Evolution Strategy: A Comparing Review*, Studies in Fuzziness and Soft Computing Vol. 192 (Springer, Berlin, 2006), pp. 75–102.
[54] A. Auger, D. Brackhoff, and N. Hansen, in *GECCO '11 Proceedings of the 13th Annual Conference on Genetic and Evolutionary Computation, 2011, Dublin, Ireland*.
[55] See also http://www.lri.fr/~hansen/cmaesintro.html.
[56] https://dcc.ligo.org/cgi-bin/DocDB/ShowDocument?docid=2974.